Montana State University

Task Report No 2

A Feasibility Study of Road Culvert / Bridge Deck Deicing Using Geothermal Energy

By:

Mehran Pourakbar (Ph.D. Student)

Kathryn Plymesser, Assistant Professor

Mohammad Khosravi, Assistant Professor

Pinar Gunyol (Graduate Student)

Adrienne Phillips, Associate Professor

Taha SEN (Undergraduate Student)

Steve Perkins, Professor

Prepared for:

Montana Department of Transportation

October 2021

Civil Engineering Department, CE

TABLE OF CONTENTS

LIST OF FIGURES

LIST OF TABLES

STANDARD CONVERSION TABLE – ENGLISH TO METRIC				
Symbol	To convert from	Multiply by	To determine	Symbol
		LENGTH		
IN	inch	25.4	millimeters	mm
FT	feet	0.3048	meters	m
YD	yards	0.9144	meters	m
MI	miles	1.609344	kilometers	km
		AREA		
SI	square inches	645.16	square millimeters	mm^2
SF	square feet	0.09290304	square meters	m^2
SY	square yards	0.83612736	square meters	m^2
A	acres	0.4046856	hectares	ha
MI^2	square miles	2.59	square kilometers	km^2
		VOLUME		
CI	cubic inches	16.387064	cubic centimeters	cm^3
CF	cubic feet	0.0283168	cubic meters	m^3
CY	cubic yards	0.764555	cubic meters	m^3
GAL	gallons	3.78541	liters	L
OZ	fluid ounces	0.0295735	liters	L
MBM	thousand feet board	2.35974	cubic meters	m^3
		MASS		
LB	pounds	0.4535924	kilograms	kg
TON	short tons (2000 lbs)	0.9071848	metric tons	t
		PRESSURE AND STRESS		
PSF	pounds per square foot	47.8803	pascals	Pa
PSI	pounds per square inch	6.89476	kilopascals	kPa
PSI	pounds per square inch	0.00689476	megapascals	Mpa
		DISCHARGE		
CFS	cubic feet per second	0.02831	cubic meters per second	$m^3/_s$
		VELOCITY		
FT/SEC	feet per second	0.3048	meters per second	m/s
		INTENSITY		
IN/HR	inch per hour	25.4	millimeters per hour	mm/hr
		FORCE		
LB	pound (force)	4.448222	newtons	N
		POWER		
HP	horsepower	746.0	watts	W
		TEMPERATURE		
°F	degrees Fahrenheit	5 X (°F – 32)/9	degrees Celsius	°C
		DENSITY		
lb/ft^3	pounds per cubic foot	16.01846	kilograms per cubic meter	kg/m^3
		ACCELERATION		
g	freefall, standard	9.807	meters per second squared	m/s^2

TO CONVERT FROM METRIC TO ENGLISH, DIVIDE BY THE ABOVE CONVERSION FACTORS.

LIST OF PARAMETERS

AM	Air Mass	Q	Heat source (or sink)
A_r	Snow free area ratio	q_e	Evaporative heat flux
$cos\theta$	Cosine of solar zenith angle	q_h	Sum of convective and radiative heat fluxes
C_p	Heat capacity at constant pressure	q_m	Latent heat of fusion of snow
$c_{p,water}$	Specific heat capacity of water	q_0	Total heat flux
$c_{p,snow}$	Specific heat capacity of snow	q_s	Total sensible heat flux
F_{sc}	Cloud coverage	s	Snowfall rate
h	Convective heat transfer coefficient	T	Absolute temperature
h_{fg}	Heat of vaporization	T_a	Ambient temperature
h_i	Cloud base height	T_{cloud}	Temperature at the base of the clouds
h_{if}	Heat of fusion of the snow	T_{dp}	Dew point temperature
h_o	Reference base height	T_{ext}	External temperature
I	Total direct incident radiation to a horizontal surface	t_f	Liquid film temperature
k	Thermal conductivity coefficient	t_h	Hour of the day
k_a	Thermal conductivity of the air	α	Solar absorptance
k_f	Thermal conductivity of the fluid	ε	Surface emissivity
L	Characteristic length	$\varepsilon_{c,i}$	Hemispherical emissivity of the cloud at the ith level
n	Normal vector on the boundary	ε_{cloud}	Cloud emissivity
n_i	Fractional area of the sky covered at the ith level	$\varepsilon_{skyclear}$	Clear sky emissivity
N_u	Nusselt number	ρ	Density
P	Station pressure	$\emptyset$	Relative humidity of the air
P_{av}	Partial pressure of water vapor in saturated air film on the surface	σ	Stefan-Boltzmann constant
P_r	Prandtl number of air	∇T	Temperature gradient
P_{wv}	Partial pressure of water vapor in ambient conditions	Γ_i	Cloud factor
q	Conductive heat flux vector		

CHAPTER 1: INTRODUCTION

The proposed research program will investigate the feasibility of the use of a ground-coupled system that utilizes heat energy harvested from the earth as a potential alternative for deicing bridge decks and culverts. The results of this research are expected to provide benefits in safety, operation, and maintenance of transportation infrastructure in the state of Montana.

This task report contains the mechanical and thermal properties of soil and concrete to be used in this study. It also describes the development and validation process of a 3D numerical model used to assess the performance of a ground-source bridge deck deicing system under different weather conditions. Chapter 2 summarizes the results of a series of lab experiments conducted to characterize the thermal properties of two different soils, sand and silt. The results will be used to select soil material for model scale testing in the Subzero Research Lab. The use of bio-mediated soil improvement, such as Microbially Induced Calcite Precipitation (MICP), on thermal properties of soils will be also investigated. Chapter 3 presents the results of a 3D numerical model developed to assess the performance of a bridge deck deicing system. The results from a series of experimental bridge deck heating experiments conducted by Bowers (2016) were used to validate the numerical model. This report concludes by a parametric study providing a basic understanding of the performance of these systems under Montana weather condition.

CHAPTER 2: SOIL CHARACTERISTICS

Index Tests and Grain Size Analyses

Soil Properties

Ottawa F-65 sand was obtained from US Silica in 2020. Ottawa F-65 sand and is classified as a whole grained silica sand. This sand is a white silica sand with rounded grains, with a quartz content of 99.7% and with little to no fines (US Silica, 2016). Ottawa F-65 sand is obtained from an area close to the Illinois and Fox Rivers near Ottawa, Illinois. The sand deposits are then mechanically processed in US Silica's Ottawa Plant facility. Sil-Co-Sil 250 silt was obtained from U.S. Silica in 2020. Sil-Co-Sil 250 is a highly granular, non-plastic silt with a quartz content of over 99.5%. The material is processed and manufactured in U.S. Silica facility. It is low in moisture, chemically inert, and acid resistant.

The specific gravity, G_s, of the sand and silt are 2.65 and 2.75, respectively (Bastidas, 2016, U.S. Silica, Price, 2018). The G_s was obtained based on the ASTM D854-14 (2014) standard method with necessary modifications. The maximum void ratio (e_{max}) of the sand was determined to be 0.83 based on the ASTM D4254-00 (2000) method. The minimum void ratio (e_{min}) of the sand was found to be 0.51 and calculated using $\rho_{d,max}$ and G_s = 2.65. $\rho_{d,max}$ and G_s were determined based on the Japanese test method for minimum and maximum densities of sand JIS A 1224 (JIS 2009) (Bastidas, 2016).

Grain Size Distribution

Dry sieve analysis (ASTM D6913-04) and hydrometer analysis (ASTM D422–63) were performed to separate particles into size ranges and specify quantitatively the mass of particles in each range. The sieve analysis was repeated for two different samples of 200 g Ottawa F-65 sand taken from a single batch. For the particle sizes smaller than 75-mm (2.95-in), the distribution of particles was determined by a sedimentation process, using a hydrometer. Hydrometer analysis tests were performed for both Ottawa F-65 and Si-Co-Sil 250. Figure 1 presents the grain size distribution curves for both Ottawa F-65 sand and Sil-Co-Sil 250.

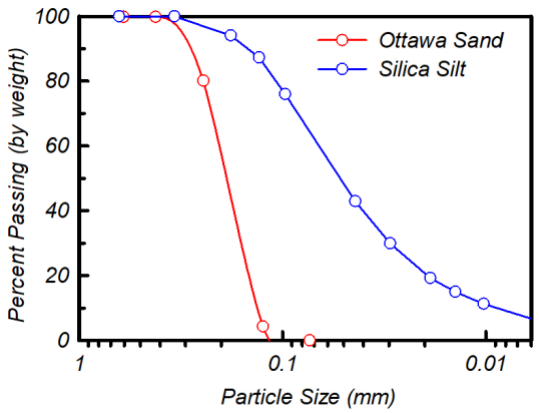

Figure 1. Grain size distribution curve for Ottawa F-65 sand and Sil-Co-Sil 250 Silt

Table 1 summarizes the data for Ottawa F-65 sand from different studies along with the data obtained in this study. The data include fines content, grain sizes corresponding to 10% (D_{10}), 30% (D_{30}), and 60% (D_{60}) finer by weight, coefficient of uniformity (C_u), coefficient of curvature (C_c), and USCS classification. Ottawa F-65 is a poorly graded sand with little to no fines, D_{10} = 0.09 mm (0.004-in), D_{30} = 0.12 mm (0.005-in), D_{60} = 0.15 mm (0.006), C_u=1.67, and C_c=1.08 and silica silt (Sil-Co-Sil 250) is a material comprised of crushed angular particles with a median particle size of approximately 0.05 mm (0.002-in).

Table 1. Summary of grain size distribution data for Ottawa F-65 sand

Author	Method	D_{60}	D_{10}	D_{30}	C_u	C_c	Fines (%)	USCS
Bastidas (2016)	Dry sieving	0.22-mm 0.009-in	0.13-mm 0.005-in	0.17-mm 0.007-in	1.61	0.96	0.2	SP
US Silica (2013)	Dry sieving	0.21-mm 0.008-in	0.14-mm 0.0055-in	0.17-mm 0.007-in	1.55	1.01	0.1	SP
This Study	Dry sieving	0.15-mm 0.006-in	0.09-mm 0.004-in	0.12-mm 0.005-in	1.67	1.08	2.64	SP

Soil Thermal Conductivity

Thermal properties of the soil were measured using a portable, battery-operated TEMPOS Thermal Properties Analyzer and a TR-3 sensor. The TR-3 sensor has a 100-mm long, 2.4-mm diameter needle that was inserted into the specimen through the cap and kept inside the column. Based on the system's manual, a minimum of 10 mm of soil material parallel to the sensor in all directions is required to avoid errors in measuring thermal properties of the soil. Thus, the specimens were prepared in columns with an inner diameter of 50-mm and a height of 120 mm and the design allowed for thermal conductivity measurements.

The soil specimens were compacted in cylindrical columns. Compaction were performed in eight lifts with moist soil distributed evenly throughout the column for each layer. To prevent excessive compaction of lower layers, Ladd's (1978) compaction method was used (Ladd,1978). The amount of soil required for each lift was determined based on the target relative density of 50%. The specimens tested for thermal conductivity were prepared with Ottawa F-65 sand and silica silt (Sil-Co-Sil 250) at %0 and %5 fine contents. Table 2 provides details of the specimens and thermal conductivity measurements under different saturation conditions.

Table 2. Summary of Thermal Conductivity Testing Specimens

Specimen	*Fine Content (%)*	*Thermal Conductivity: Initial Condition (W/m.K)*	*Thermal Conductivity: Saturated (W/m.K)*
F0-1	0	1.7	2.5
F0-2	0	1.8	2.5
F5-1	5	2.1	2.6
F5-2	5	2.0	2.5

It can be seen in Table 2 that the initial values of k_t for the specimens increased between 11-21% when the specimens were prepared with 5% fine content. After the soil specimens were saturated with deionized water, their thermal conductivity significantly increased. The difference in thermal conductivity between F0 and F5 specimens was less prominent under saturated conditions. This was expected as the thermal conductivity of the soil increases with the degree of saturation as the air in voids is replaced with water. Heat transport and therefore thermal conductivity could be greatly influenced by interparticle interactions and the presence of liquids in pores, and the ordered sequence of typical soil related thermal conductivity values are: $k_{air} < k_{dry-soil} < k_{water} < k_{saturated-soil} < k_{mineral}$ (Yun & Santamarina, 2007).

CHAPTER 3: CONCRETE MIX DESIGN

Concrete is a mixture of water, cement, fly ash, slag (ground granulated blast-furnace slag cement, GGBFS, for the cases), and other cementitious materials (CM). CMs are one of the principal ingredients of concrete mixture which are used in conjunction with Portland cement to reduce the heat of hydration, improve the workability of concrete mixture, and reduce thermal cracking in structures. The most known cementitious materials are fly ash, slag, and silica fume. Fly ash has numerous assets in both the hardened and the fresh state of concrete. Fly ash use in concrete is cost-effective as it reduces the amount of cement in the mix design. It also improves workability of the concrete mixture and strength and durability of the concrete after it has cured. Slag is one of the most utilized cementitious materials in concrete, both as a part of blended cement and separate cementitious material. It works with Portland cement to enhance strength and durability of concrete against chemicals and reduce permeability, and corrosion of rebars. Silica fume, an excessive pozzolanic material, provides early high compressive strength, high tensile strength, durability, toughness, abrasion resistance, and high electrical resistivity; and decreases permeability.

The objective of this chapter is to assess the mechanical and thermal properties of concrete to be used in this study. To design the concrete mixture for the model-scale bridge deck and culvert experiments, a series of concrete mix designs approved by Montana Department of Transportation (MDT) was collected. In this section, a summary of the collected data is presented, and the procedure used to design the concrete mixture for the model-scale experiments in the Subzero Research Lab (SRL) at MSU is discussed.

An Overview of the Collected Mix Designs

Table 3 illustrates the amount and percentages of concrete aggregates used in the concrete mix designs approved by MDT. It also indicates gradation types for each concrete mixture. Concrete aggregates used in these mixtures include sand in the range of 36.5% to 44.2%, coarse aggregate (CA) in the range of 49.2% to 56.7%, and fine aggregate (MA) in the range of 10.1% to 14.3% (in mixtures 1811DECK04 and 2022STRUCTURE02).

Table 3. Gradation and Gradation Properties of Concrete Mix Designs' Aggregates

Sample ID	*Unit*	*Sand #1*	*Sand #2*	*CA #1*	*CA #2*	*CA #3*	*MA #1*	*Gradation Type*
1811DECK04	*lbs.*	1100	-	-	1480	-	430	Optimized
	%	36.5%	-	-	49.2%	-	14.3%	
1931DECK01	*lbs.*	1320	-	1730	-	-	-	Conventional
	%	43.3%	-	56.7%	-	-	-	
1943DECK01	*lbs.*	1380	-	1740	-	-	-	Conventional
	%	44.2%	-	55.8%	-	-	-	
2022STRUCTURE02	*lbs.*	1220	-	1527	-	-	310	Optimized
	%	39.9%	-	50.0%	-	-	10.1%	
2031DECK01	*lbs.*	1320	-	1730	-	-	-	Conventional
	%	43.3%	-	56.7%	-	-	-	

CA: coarse aggregate, MA: fine aggregate.

Cementitious Materials

Table 4 summarizes the weights and percentages of the cementitious materials used in the concrete mix designs approved by MDT. The specific gravity of cement is typically 3.15. As shown in Table 4, in addition to cement, slag (1811DECK04) and fly ash (1931DECK01, 1943DECK01, and 2031DECK01) in the range of 15% to 20.0%, and Silica Fume, type 100, (all mixtures but 2022STRUCTURE02) in the range of 4.0% to 5.0% have been used in these mixtures.

Table 4. Ingredients of the Collected Concrete Mix Designs

Sample ID		*Cement*	*Fly Ash*	*GGBFS*	*Other CM*	*Water (lb)*	*W/C*
1811DECK04	*lbs.*	426	-	113	25	242	0.43
	%	78.0%	-	20.0%	5.0%		
1931DECK01	*lbs.*	430	90	-	30	231	0.42
	%	78.0%	16.0%	-	5.0%		
1943DECK01	*lbs.*	454	85	-	25	235	0.42
	%	80.0%	15.0%	-	4.0%		
2022STRUCTURE02	*lbs.*	580	-	-	-	217	0.37
	%	100.0%	-	-	-		
2031DECK01	*lbs.*	430	90	-	30	231	0.42
	%	78.0%	16.0%	-	5.0%		

GGBFS: ground granulated blast-furnace slag, CM: cementitious material, W/CM: water/cement

Admixtures

Table 5 illustrates the targeted air content, slump height, and volume of the admixtures used in the MDT approved concrete mixtures. Admixtures are utilized in a concrete mixture to reduce the water content in a mixture, reach a specific slump, slow the setting rate of the concrete while retaining the flowing properties of a concrete mixture, accelerate early-strength improvement, reduce air bubbles to increase cohesion, decrease freeze-thaw breakdown, etc. Mid-range and high-range air-entraining agents (admix #1) and mid-range and high-range water-reducing agents (admix #2) have been used in all the concrete mixtures. Additionally, high-range water-reducing agents (admix #3) have been used in 1811DECK04, 1931DECK01, and 2031DECK01. Lastly, workability-retaining agent (admix #4), which are for slump retention, was utilized in 1811DECK, and 1931DECK01, while hydration controlling agent (admix #5) has been utilized only for 1811DECK04.

Base Mix Design

Two candidate mixtures are proposed here for the model-scale experiments in the SRL, one with 100% Portland cement (similar to mixture 2022STRUCTURE02), and one with 85% Portland cement and 15% fly ash (similar to mixtures 1931DECK01, 1943DECK01, and 2031DECK01). Water/cement ratio of the recommended mixtures was 43% for the mixture with fly ash and 37% for the mixture without fly ash. The mix proportions for a 2.5 cu. ft mix are provided in Table 6.

The mix designs used cement from the Trident cement plant, and fly ash from the Genesee Generating Station. No admixture was used in the concrete mix design in this study.

Table 5. Aim of Air Contents, and Admixtures' Dosages of the Collected Mix Designs

Sample ID	*Admix #1 Dosage*	*Admix #2 Dosage*	*Admix #3 Dosage*	*Admix #4 Dosage*	*Admix #5 Dosage*	*% Air Content*
1811DECK04	0.8 oz/100# CM	5 oz/100# CM	8 oz/cy	2 oz/cy	45 oz/cy	6
1931DECK01	1-2 oz/100# CM	5-6 oz/100# CM	4-8 oz/100# CM	2-6 oz/100# CM		5.0-8.5
1943DECK01	0.8 oz/100# CM	6 oz/100# CM				6
2022STRUCTURE02	3.2 oz/cy	46 oz/cy				7.1
2031DECK01	1-2 oz/100# CM	6 oz/100# CM	6 oz/100# CM			7

Table 6. Mix Proportions for 2.5 cu. ft. Mix

Item	***Item Type***	***Amount (lbs)***	
		W/O Fly Ash	***With Fly Ash***
Water	-	19.8	21.4
Portland Cement	Type I/II Trident	52.9	41.4
Fly Ash	Trident Genesee	-	7.7
Fine Aggregate	O.D. BBB&T Concrete Sand	111.2	125.8
Coarse Aggregate		139.2	158.6
W/C ratio (%)	-	*37*	*43*

Two different concrete aggregates obtained from Bozeman Brick and Tile and Bekaert Steel Fibers were used. For each aggregate used in the mix design, a gradation analysis that is representative of the aggregates was performed and the individual grain size distribution curves are presented in Figure 2. For the combined aggregate, the ratio used in the mixtures 1931DECK01, 1943DECK01, and 2031DECK01 with a conventional gradation type was utilized. As shown in Table 3, the percentages of the coarse and fine aggregates in these mixtures were 56% and 44%, respectively.

Concrete Aggregate Combined Gradation

Three optimization charts are required to be incorporated into the concrete mix design: 1) Coarseness Factor chart, 2) 0.45 Power chart, and 3) Percent Retained chart. Each chart represents one aspect of an optimized aggregate gradation. The coarseness factor chart (i.e., The Shilstone Chart) is a method for determining if the combined aggregate gradation is considered optimized. The chart helps describe the relationship between coarseness factor and workability factor of a concrete mix. The coarseness factor (x-axis) and workability factor (y-axis), which are both in percentage, can be calculated as Equations (2) and (3), respectively:

$$CF\ (\%) = \frac{Q}{R} \times 100 \quad (1)$$

$$WF\ (\%) = W + \frac{2.5 \times (C - 564)}{94} \quad (2)$$

where Q is the cumulative % retained on a 3/8" sieve, R is the cumulative % retained on the No. 8 sieve, W is the percent passing the No. 8 sieve, and C is the cementitious material content in lb/yd³.

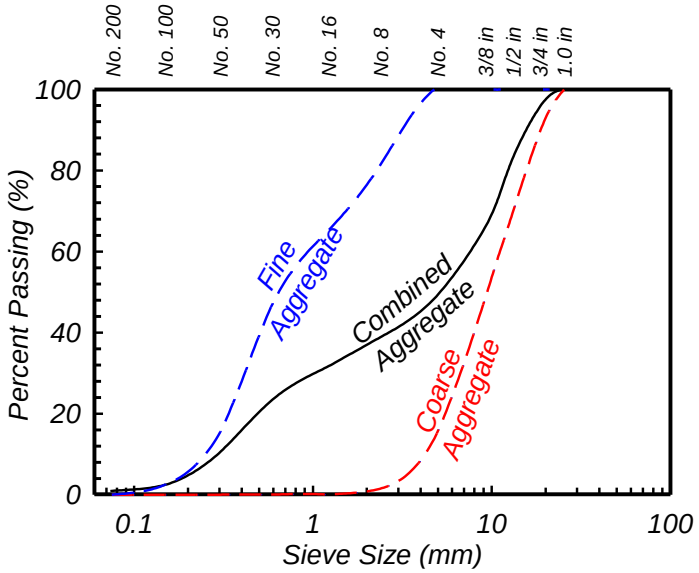

Figure 2. Individual Grain Size Distribution Curves

Figure 3 illustrates the coarseness factor chart for the proposed concrete mix designs. Zone II is generally considered as the zone of reasonable mix. Combined aggregates that plot near the boundaries of or outside Zone II are more prone to problems either during placement or in overall durability. As shown here, both combined aggregates fall into Zone II. The concrete mix with fly ash plots on the boundaries of the workability box, while the mix without fly ash fall outside the box suggesting that the mix with fly ash has a better workability.

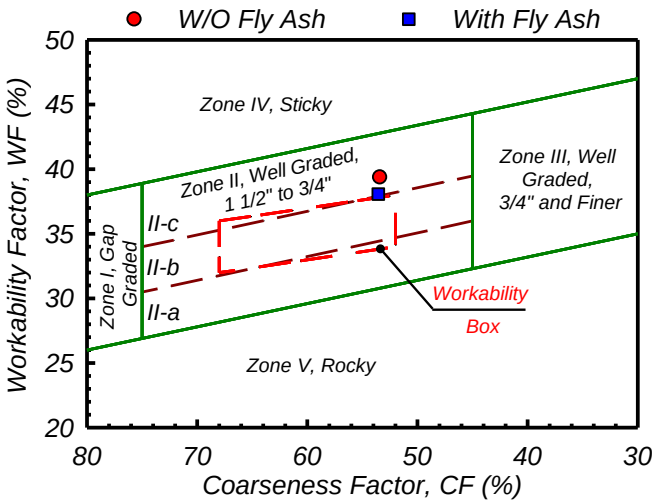

Figure 3. Coarseness Factor Chart of Concrete Mix Designs

The 0.45 power line is one of the methods used for predicting voids in the concrete's combined aggregates. In Figure 4(a), the 0.45 power line is developed in accordance with the nominal maximum size of the combined aggregates. A gradation line that passes above the line represents fine aggregates; below the line represents coarse aggregates. Figure 4(a) shows the grain size distribution of the combined aggregates and the power line. As shown here, the grading curves for the portion of the combined aggregate passing the No. 30 sieve falls primarily below the power chart line allowing space for the cementitious materials in the final mix. As shown in this Figure 11(a), the combined grading is within ± 7 percentage points of the Power Chart line.

Individual percent retained chart (i.e., Haystack Plot) is a method to describe the excess or lacking combined aggregate sizes in the mixture. The chart can also be used to identify workable mixes with a reasonably low water demand. Plots are restricted with high and low lines. The boundaries of the high line and the low line are generally between 18-22% and 5-12%, respectively. To prevent segregation, it is generally recommended to have at least a total of 13% of the combined aggregate retained on any two adjacent sieves. Figure 4(b) demonstrates the percent retained on each sieve (y-axis) of the concrete mix design in each sieve size. The upper limit is 20% and the lower limit is 8% in this case. As shown here, the concrete mix is between the "High" and "Low" line, suggesting that the mix is workable and has a reasonably low water demand.

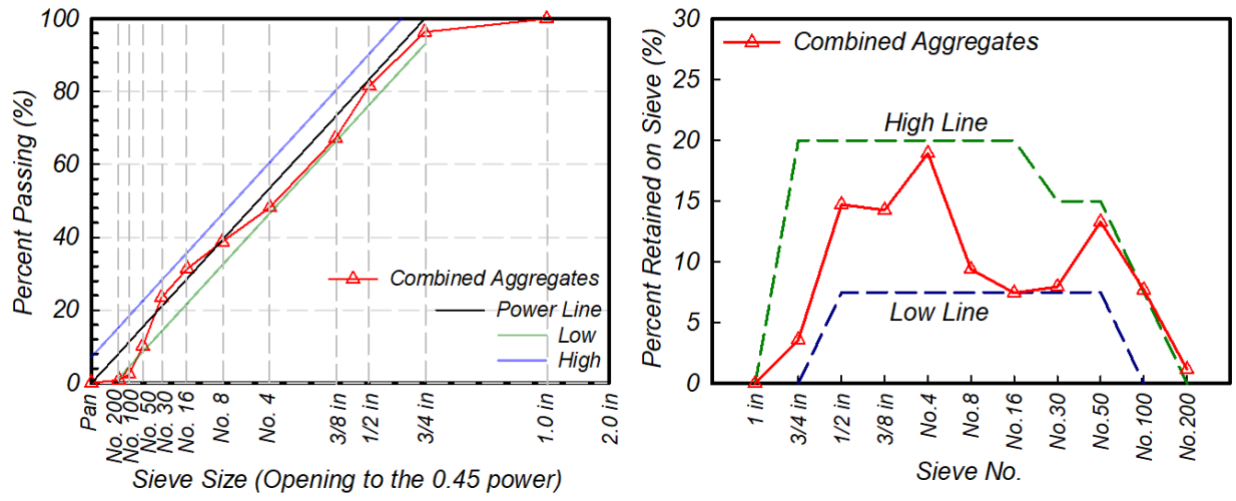

(a) *(b)*

Figure 4. a) 0.45 Power Chart, and b) Percent Retained Chart of the Collected Mix Designs

Average 7- and 28-day compressive strengths are summarized in Table 7. Compressive strength tests were conducted in accordance with ASTM D-1633. The compressive strength of the MDT concrete mix designs were in the range of 3200 to 4200 psi for the 7-day curing time and 4990 to 5500 psi for the 28-day curing time. For the recommended concrete mixtures, a 7-day strength in the range of 2600 psi to 4000 psi was obtained, while the 28-day strength was in the range of 3400 psi to 4700 psi. The results were comparable to those approved by MDT. The results suggested that using fly ash as cementitious material could result in a lower strength, therefore, the mixture without fly ash will be used for the model-scale experiments. Figure 5 shows the concrete samples after failure.

Table 7. Average Compressive Strengths of the Collected and Proposed Concrete Mix Designs

Sample ID		***Fly Ash (%)***	***Compressive Strength (psi)***	
			7-day	***28-day***
Collected	*1811DECK04*	*0.0*	*3457*	*4990*
	1931DECK01	*16.0*	*4110*	*5547*
	1943DECK01	*15.0*	*3233*	*5237*
	2022STRUCTURE02	*0.0*	*4140*	*5440*
	2031DECK01	*16.0*	*4150*	*5210*
Proposed	*W/O Fly Ash*	*0.0*	*3967*	*4659*
	With Fly Ash	*15.0*	*2666*	*3471*

(a) *(b)*

Figure 5. Two proposed Concrete Mixtures after 28-day Strength Test

Slump Test

Table 8 summarizes the results of slump tests for a specified temperature, air content, unit weight, and yield. Slump tests measure the workability and consistency of the concrete mixture when it is fresh. Slump tests have been conducted in accordance with ASTM C-143.

Table 8. Properties of Proposed Concrete Mixture Designs

Sample ID	***Fly Ash (%)***	***Slump (in)***	***Air (%)***	***Temperature (^oF)***	***Unit Weight (pcf)***	***Yield (yd^3)***
1811DECK04	*0.0*	*5.0*	*6.1*	*63*	*141.1*	*27.2*
1931DECK01	*16.0*	*5.0*	*7.1*	*60*	*141.1*	*27.1*
1943DECK01	*15.0*	*4.0*	*8.5*	*70*	*139.7*	*-*
2022STRUCTURE02	*0.0*	*4.0*	*6*	*60*	*143.1*	*27.1*
2031DECK01	*16.0*	*3.5*	*7.3*	*68*	*140.1*	*27.8*
W/O Fly Ash	*0.0*	*5.0*	*-*	*-*	*-*	*-*
With Fly Ash	*15.0*	*1.7*	*-*	*-*	*-*	*-*

Thermal Conductivity and Resistivity

Thermal properties of the tested concrete were measured using a portable, battery-operated TEMPOS Thermal Properties Analyzer and TR-3 sensor with a 100-mm long, 2.4-mm diameter needle (Figure 6). The probe (analyzer) and the sensor follow ASTM 5334 and IEEE442 standards.

The concrete specimens were prepared with a diameter of 100-mm (4 inches) and a height of 200 mm (8 inches). Based on the system's manual, a minimum of 10 mm of concrete material parallel to the sensor in all directions is required to avoid errors in measurement

Figure 6. Thermal Test Setup

Thermal properties of the concrete mixtures were measured under two different conditions: 1) fresh condition, and 2) after 7 days of curing. To measure the thermal properties of the cured sample, a 4-mm (5/32 in) hole was drilled in the concrete with a rotary hammer. The hole was cleaned with compressed air and filled with thermal grease (Arctic Silver 5 AS55-3.5G). The thermal greased was used to increase the dissipation of the heat in samples and provide a good thermal contact between the sensor and concrete. The sensor needle was then inserted into the hole. The thermal properties of the concrete were only measured after 7 days of curing as drilling a hole in a 28-day cured concrete sample was too difficult. Table 9 summarizes the thermal properties of the concrete before and after curing.

Table 9. Thermal Conductivity of Proposed Concrete Mix Designs

Sample ID	***Fly Ash (%)***	***Thermal Conductivity (J/S/m^2)***	
		Fresh concrete	***7-day curing***
W/O Fly Ash	*0.0*	*1.489*	*1.927*
With Fly Ash	*15.0*	*-*	*1.796*

The thermal conductivity of the concrete depends on water content, size and type of aggregates, and density of the material. The thermal property of a saturated concrete sample is typically in the range of 1.4 to 3.4 J/S/m^2.

CHAPTER 4: NUMERICAL MODEL CALIBATION

Introduction

In Task Report 1, an overview of the application of geothermal energy for bridge decks and culvert deicing was presented. Case studies, model scale lab experiments, and numerical modeling of shallow geothermal foundations were summarized to evaluate recent advances in Ground Source Heat Pump (GSHP) systems. Following the literature review, a three-dimensional numerical model was developed to further study the feasibility of a hydronic heating system for deicing bridges. The numerical model was then validated using the results of the experimental tests conducted by Bowers (2016). This chapter will present an overview of the experiments performed at the Virginia Tech Geotechnical Research Facility by Bowers (2016), a description of the numerical simulation of a bridge deck snow melting/de-icing system, and validation results.

Overview of the Experiments (Bowers, 2016)

The thermal performance of a small-scale bridge deck deicing system was investigated by Bowers (2016) at the Virginia Tech Geotechnical Research Facility. Two bridge deck models were constructed (1.3 m (4.3 ft) wide, 3.05 m (10 ft) long, and 0.254 m (10.4 inch) deep). The experimental deck models are shown in Figure 7(a). The heat exchanger pipes had a spacing of 30 cm (12 inch) and 20 cm (8 inch) in the left-side and right-side of the model deck, respectively. The inner and outer diameter of the pipes was 16 mm (0.62 inch) and 22 mm (0.87 inch), respectively. The circulating fluid was a 20% glycol solution with a flow rate of 15.1 L/m (1.2 gal/ft). The operation of the systems was monitored with several temperature sensors installed in the decks. Several thermistors were placed inside the deck to measure deck temperatures. Figure 7(b) and (c) show the plan view and cross-sectional view of the sensor locations. Virginia Department of Transportation (VODT) class A4 concrete mixture was used in the bridge deck models. Class A4 concrete has a minimum 28-day compressive strength of 27.6 MPa (4000 psi) and is expected to have a maximum permeability of 2500 coulombs. Figure 8 shows the experimental deck models after pouring the concrete into the two halves of the deck.

Experimental Program

Various weather conditions were tested in the Bowers (2016) study including: 1) a severe winter event to explore the effect of material properties and the lower surface boundary condition on the heating process of the deck, and 2) a period of cold weather followed by snowfall. The latter weather condition helped examine; 1) the boundary conditions of the model as the deck was clear during the initial part of the test and subject to radiation and convection with the environment, and 2) the snowmelt model as the snow is falling. These test conditions were selected based on the weather conditions in the project site (Blacksburg, Virginia) and Montana. Table 10 summarizes the selected weather parameters and experimental results of snow melting.

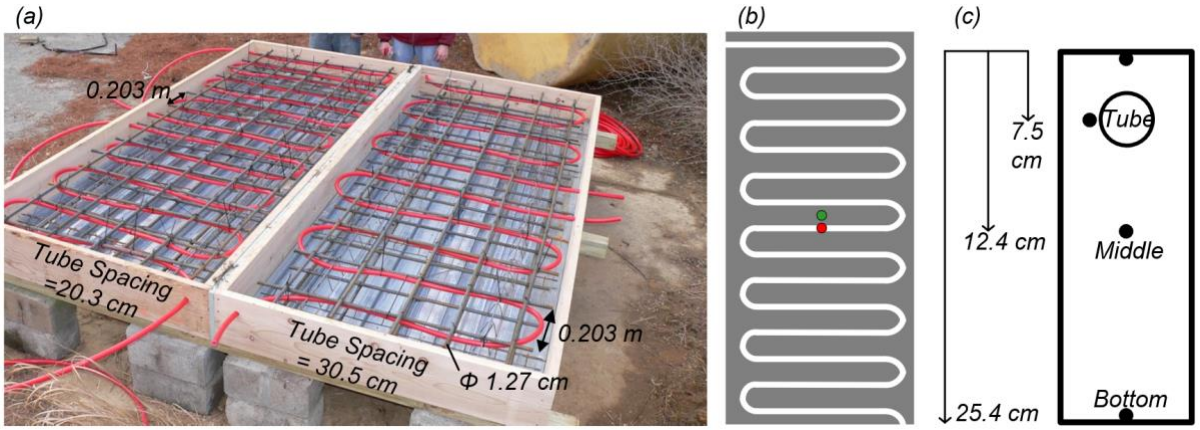

Figure 7. (a) Layers of reinforcement and the configuration of heat exchanger pipes, (b) Location of studied temperature sensors (plan view), and (c) Location of studied temperature sensors deck (cross section) (Bowers, 2016)

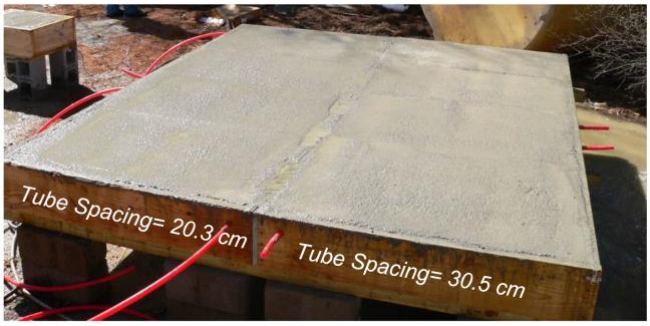

Figure 8. Photograph showing the poured concrete into the deck frame works (Bowers, 2016)

Table 10. Selected weather parameters and experimental test results of snow melting

Cold event (time)	***Severe winter event (20-23 February 2015)***	***Moderate winter event (25-27 February 2015)***
Ambient temperature (°C)	-18 to 10 (-0.4 °F to 50 °F)	-7 to 6 (19.4 °F to 42.8 °F)
Depth of snow (cm)	20 (7.87 inches)	7.6 (3 inches)
Starting time of operation	14:30, 2/20/2015	In operation
Circulating fluid temperature (°C)	3.8 to 7.2 (38.8 °F to 45.0 °F)	6 to 9.6 (42.8 °F to 49.3 °F)
Melting time (Hours)	48.5	31.5

Severe Winter Weather (February 20-22, 2015)

On February 16-17, 2015, a snowstorm occurred in Blacksburg, VA. During this time, the system was non-operational, and almost 20 cm (7.87 inch) of snow accumulated on the surface. Variation of top surface temperature of heated and non-heated decks, air temperature, cumulative snowfall, and deck surface conditions during heating operation are shown in Figure 9. Heating of the bridge deck started after the snowstorm, at 14:30 on February 20, 2015. The temperature of the deck surface was -18 °C (-0.4 °F) when heating was initiated. Figure 9(a) was taken after 2.5 hours of system operation, at 17:00 on February 20, 2015 prior to further snowfall on February 21, 2015.

At that time, the measured snow depth was 16.5 cm. After 9 hours of heating, the average surface temperature of the model deck was above the freezing point despite an ambient temperature drop of 15 °C (59 °F). Figure 9(b) shows the deck surface condition after 19.5 hours, at 10:00 on February 21, 2015. The heated-deck surface temperature remained above the freezing point during the entire storm. The recorded snow depth on the non-heated and heated decks was 22.9 cm (9 inch) and 20.3 cm (8 inch), respectively. One hour later, the snow depth on the non-heated deck reached a maximum of 24.1 cm (9.5 inch), while the recorded snow depth on the heated side was 19.7 cm (7.7 inch). This observation indicated that the rate of snow melt was greater than the rate of snow accumulation. After 24.5 hours of operation, at 15:00 on February 21, 2015, the measured snow depth on the heated and non-heated deck was 29.8 cm (11.7 inch) and 24.1 cm (9.5 inch), respectively, as shown in Figure 9(c). After 29 hours of system operation, at 19:30 on February 21, 2015, the recorded snow depth on the non-heated and heated deck was 30.5 cm (12 inch) and 21.6 cm (8.5 inch), respectively. The results also indicated that the rate of snow melting increased as the ambient temperature increased. In Figure 9(d), which was taken after 41 hours, at 7:30 on February 22, 2015, the measured snow depth was 11.4 cm (4.5 inch) on the heated deck. Figure 9(e) indicates the deck surface condition after 48.5 hours of heating system operation, at 15:00 on February 22, 2015. As can be seen, the system was able to keep the deck free from snow at that point in time. It should be also noted that the deck surface temperature suddenly raised when the surface was cleared of snow.

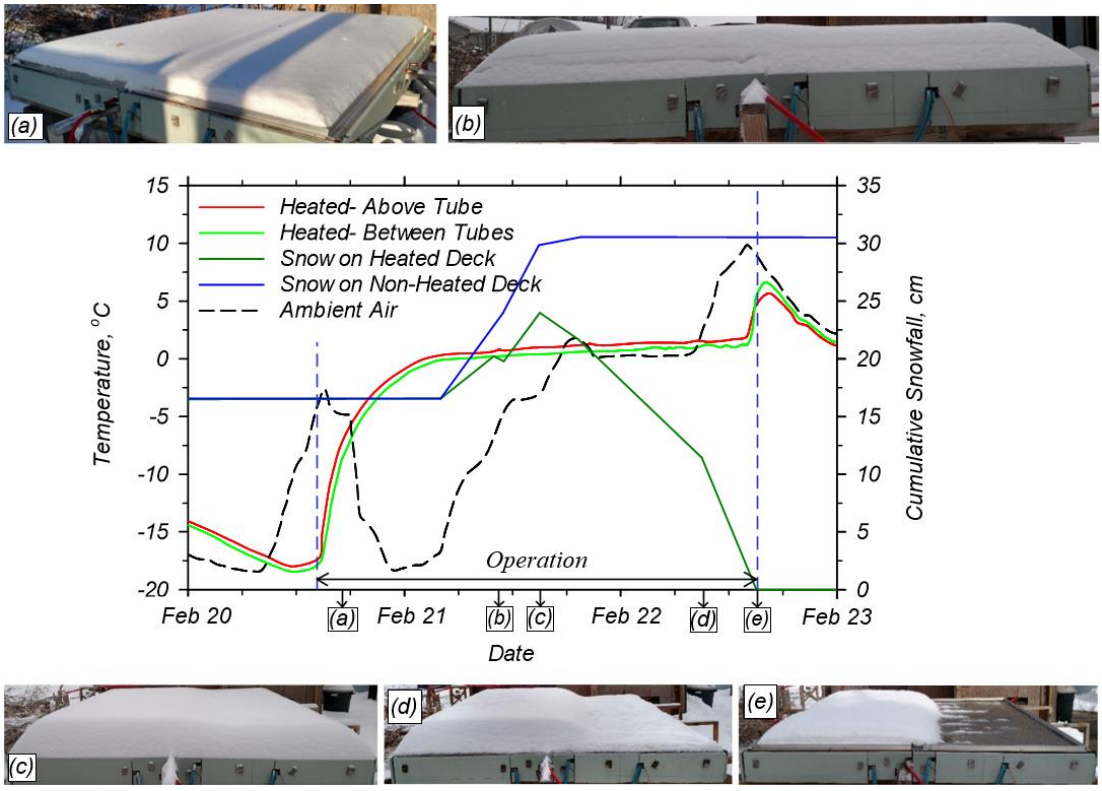

Figure 9. Recorded surface temperature of the heated and non-heated decks, ambient temperature, cumulative snowfall, and photo of the deck model surface during the storm after: (a) 2.5 hours (b) 19.5 hours, (c) 24.5 hours, (d) 41 hours, (e) 48.5 hours of heating system operation (Bowers, 2016)

Moderate Winter Event (February 25-26, 2015)

Bowers (2016) studied the performance of the bridge deck deicing system in response to a moderate storm that occurred on February 25-26, 2015. The surface temperature of the heated and non-heated decks, ambient air temperature, cumulative snowfall, and the model deck surface condition during the experiment are shown in Figure 10. The system in the heated side was turned on before this cold event occurred. The results of the recorded ambient temperature indicated that the ambient temperature varied between -7 °C (19.4 °F) and 6 °C (42.8 °F) during the system operation. As shown in Figure 10, during an average ambient temperature of -2.5 °C (27.5 °F), 7.6 cm (3 inch) of snow fell.

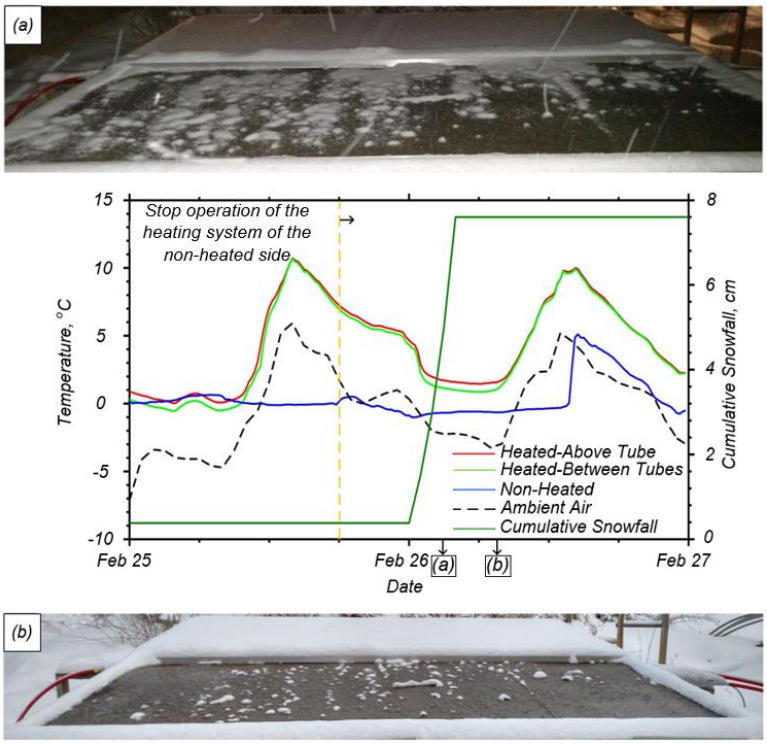

Figure 10. Recorded surface temperature of the heated and non-heated decks, ambient temperature, cumulative snowfall, and photo of the deck surface condition during the test: (a) 2.5 hours, and b) 7.5 hours after the storm began (Bowers, 2016).

Figure 10(a) was taken 2.5 hours after the storm began, at 2:30 on February 26, 2015. The results indicated that the system could maintain deck surface temperatures above the freezing point (0 °C (32 °F)) during the entire storm. As reported by Bowers (2016), at this time, 60 % of the heated deck surface was free of snow, indicating that the system was able to prevent snow accumulation on the surface. The further inspection revealed that about 50 % of the accumulated snow was due to the debris blown onto the deck by the wind. The other 50 % was accumulated in areas between the heat exchanger pipes. As the results indicated, the surface temperature of the non-heated deck dropped the below freezing point, which resulted in accumulation of snowfall on the surface. Figure 10(b) illustrates the deck surface condition at 7:30 on February 26, 2015, 7.5 after the storm.

In the heated side, there was no snow on the deck surface. In contrast, the non-heated deck surface was covered with snow. The recorded snow depth on the non-heated deck was 7.6 cm.

Numerical Simulation of Bridge Deck Snow Melting/De-icing System

In this section, the relevant heat sources and heat transfer mechanisms in the process of bridge deck heating and de-icing are discussed. Then the numerical model calibration using the results of the experimental tests conducted by Bowers (2016) are presented. Model development and appropriate boundary conditions are described in detail in the Model Validation section.

Bridge Deck Heating and Snow Melting Process

Modeling the bridge deck deicing process is complicated due to the involvement of different heat transfer mechanisms and changes in weather condition during the operation of bridge deck heating systems. Figure 11 illustrates a schematic of the main contributing heat transfer mechanisms in geothermal bridge systems. Heat transfer with the surroundings may happen through four major mechanisms: *conduction, convection, radiation (solar and thermal radiation), and precipitation heat flux.*

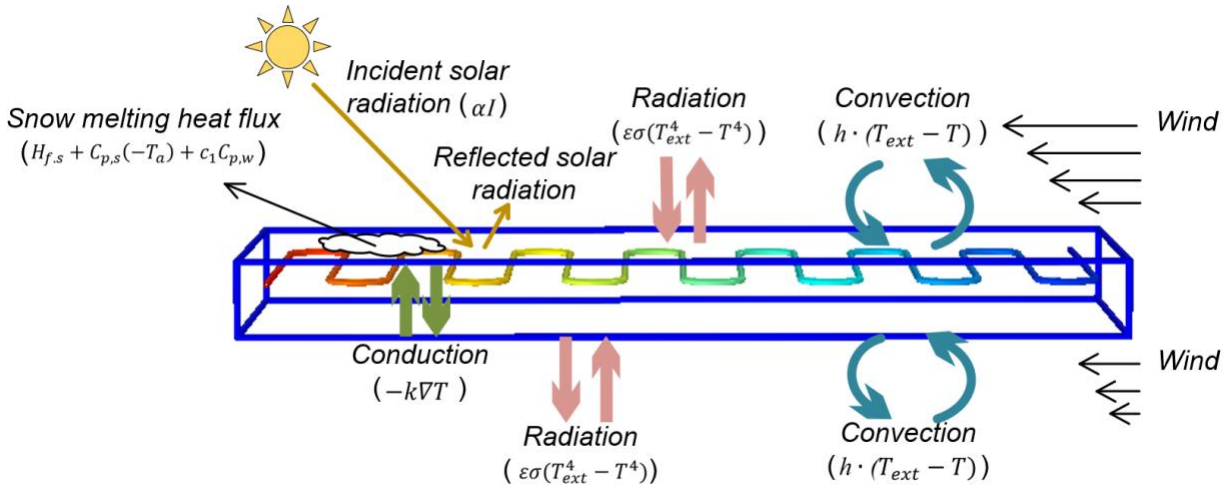

Figure 11. Heat transfer mechanisms involved in bridge heating and snow melting process

Conductive Heat Transfer

Heat transfer by *conduction* refers to a transfer of energy from more energetic particles to less energetic particles arising from a temperature gradient (Thompson, 2013). In a bridge deck de-icing system, conduction occurs between the heat exchanger fluid and pipe walls and between the pipe and surrounding concrete. Equation (4) presents the differential equation in heat conduction in solids.

$$\rho C_p \frac{\partial T}{\partial t} + \nabla . q = Qq = -k\nabla T \quad (3)$$

where ρ is the density (kg/m^3), C_p is the heat capacity at constant pressure (J/(kg.K)), T is the absolute temperature (K), $\frac{\partial}{\partial t}$ is time derivatives operator, q is conductive heat flux vector (W/m^2), k is the thermal conductivity coefficient (W/m·K), ∇T is the temperature gradient, and Q is the heat source (or sink) (W/m^3). The relationship between the heat flux vector and temperature gradient is defined by the thermal conductivity coefficient in $q = -k\nabla T$, which is Fourier's law of heat conduction. The heat flux at a surface is equal to zero for insulated boundary conditions (e.g., insulation effect of any snow accumulation on the bridge deck surface from heat loss). Equation (5) defines the governing equation in this condition.

$$q = (-k\nabla T) = 0 \tag{4}$$

Convective Heat Transfer

Heat transfer occurs by *convection* through the fluid's bulk motion (Brandl, 2006). Heat transfer by convection can occur by either a natural or forced nature of the flow. Natural convection occurs when there is no forcing by any external agency. In natural convection, motion and therefore heat transfer occurs due to temperature or concentration gradient. Forced convection occurs by any external means (i.e., wind or Groundwater flow). Heat convection can occur in the bridge deck de-icing system on any surface exposed to the atmosphere and from the circulating fluid to the heat exchanger pipe wall. Heat transfer by convection is modeled by Newton's law of cooling which is expressed as Equation (6):

$$-n.\,q = \mathrm{h} \cdot (T_{ext} - T_s) \tag{5}$$

where n is the normal vector on the boundary, h is the convective heat transfer coefficient (W/m^2 ·K), T_s is the surface temperature (K), and T_{ext} is the external temperature. T_{ext} for the top and bottom surfaces is either ambient temperature or mean radiant temperature (K). Determination of the convective heat transfer coefficient depends on the boundary layer (i.e. wind speed and ambient temperature), the nature of the fluid movement, and fluid properties (Chowdhury, 2019). According to Williams (1973), adjustment of the convective heat transfer coefficient is essential based on the size of the heat transfer area, exposure to wind, and the height at which the wind speed is measured.

Radiative Heat Transfer

Heat propagation through *radiation* occurs in pore spaces due to the motion of electromagnetic waves or alternatively by photons. Heat transfer by radiation is important in bridge heating. Several factors, including the ambient temperature, cloud coverage, surface emissivity, latitude and longitude of the studied area, time of day, and time of year, could affect the amount of energy that is released or absorbed by radiation in a hydronic heating system. The radiative out-of-plane heat flux is calculated by Equation (7):

$$-n.\,q = \varepsilon\sigma(T_{ext}^4 - T_s^4) \tag{6}$$

where ε is the surface emissivity, σ is the Stefan-Boltzmann constant (a predefined physical constant, 5.67×10^{-8} (W.m^2)/K^4), T_{ext} for the top and bottom surfaces is either ambient temperature

or mean radiant temperature (K). To compute the longwave thermal radiation, an accurate determination of T_{ext} is necessary. The conditions that need to be considered in calculating T_{ext} are described in subsequent sections.

Snow Melting Heat Flux

Mathematical approaches for describing the snow melting process, including steady-state and transient models, have been proposed by several researchers (e.g., Chapman et al., 1952; Rees et al., 2002, Liu, 2005; Wang and Chen, 2009). Chapman et al. (1952) proposed a one-dimensional steady state model for computing the amount of heat that is required for snow melting. Recent studies accounted for transient snow melting processes in evaluation of the performance of a bridge deck under realistic operating conditions. Rees et al. (2002) presented a transient two-dimensional model coupling heat and mass transfer process during the snow melting process. Top surface condition in the model proposed by Rees et al. (2002) could be defined in each time step by computing the mass of snow, ice, and liquid. Due to complexity of calculations for the top surface conditions, Liu (2005) enhanced the Rees's (2002) model considering a wide variety of weather conditions and developed a more computationally efficient model. Further, Wang and Chen (2009) developed a theoretical snow melting model to include the capillary effect inside the snow layer when computing the variation of thermal conductivity of a melting snow layer.

In this study, the approach proposed by Chapman et al. (1952) was used to estimate the snow melting heat flux. Even though the model may have limitations in replicating the entire snow melting processes, it still provides a good estimation of the heat required to melt falling or accumulated snow on the deck surface. The formulation of the proposed model for total heat flux (q_0) required at the top surface of bridge deck is expressed mathematically as Equation (8):

$$q_0 = q_s + q_m + A_r(q_h + q_e) \tag{7}$$

where q_s is the total sensible heat flux (W/m^2), q_m is the latent heat of fusion of snow (W/m^2); A_r is snow free area ratio; q_h is the sum of convective and radiative heat flux (W/m^2); and q_e is the evaporative heat flux (W/m^2).

The sensible heat flux is the energy required to increase the snow temperature, which is assumed to fall at ambient temperature, to the freezing point and subsequently increase the temperature of the melted snow to the assigned liquid film temperature. The corresponding sensible heat flux (q_s) can be obtained as Equation (9):

$$q_s = \rho_{water}\, s\, [c_{p,snow}\, (t_s - T_a) + c_{p,water}\, (t_f - t_s)] \tag{8}$$

where ρ_{water} is the density of water (kg/m^3), s is the snowfall rate in expressed in water equivalent (m/s), $c_{p,snow}$ is the specific heat capacity of snow (J/(kg.K)), t_s is the melting temperature (0 °C), T_a is the ambient temperature (°C), $c_{p,water}$ is the specific heat capacity of water (J/(kg.K)), and t_f is the liquid film temperature (°C). According to ASHRAE 1999, the temperature of the liquid film is usually taken as 0.56 °C (33 °F).

The heat flux required to be absorbed during the phase change, latent heat of fusion of snow (q_m), is expressed by Equation (10):

$$q_m = \rho_{water}\, s\, h_{if} \tag{9}$$

where h_{if} is the heat of fusion of the snow, usually taken as 3.3×10^5 J/kg.

Under snow-free conditions, the heat is being transferred from the surface to the atmosphere through convection and radiation (q_h) mechanisms. These terms have been previously described in detail. The energy required to evaporate water from the surface (q_e) is defined as Equation (11):

$$q_e = (530.84V + 649.61)(P_{wv-}P_{av})\, h_{fg} \tag{10}$$

where V is the wind speed (m/s), P_{wv} is partial pressure of water vapor in ambient conditions (Pa), taken as 636.6 kPa P_{av} is partial pressure of water vapor in saturated air film on the surface (Pa), taken as 613.28 kPa,, and h_{fg} is the heat of vaporization (J/kg) (enthalpy difference between saturated water vapor and saturated liquid water), taken as 2.257 J/kg.

The snow free area ratio (A_r) in the equation presented by Chapman et al. (1952) represents the ratio of the uncovered, or free, area to the total pavement area. A_r=1 represents a snow-free surface condition, and A_r=0 means the entire surface is covered with the snow.

A few assumptions must be considered to use the Chapman et al. (1952) equation. The assumptions applied by Bowers (2016) in the use of the Chapman et al. (1952) equation are as follows. A description of the errors that resulted from these assumptions in the calculation of snow melting heat flux and the related correction methods can be found in the study by Bowers (2016).

1) All three processes of snow melting, heating the snow to freezing, melting, and heating the liquid film, happen instantaneously.
2) The melted snow will be heated to a specific point and will then disappear (perfect drainage).
3) Material and thermal properties of snow are independent of time and space.

Bowers (2016) outlined the snow melting system performance during a given snowstorm and how different conditions are related to the applied heat flux at the surface of the deck. As stated, if the energy transferred to the deck surface was enough to melt the snow as the snow hit the deck surface, the snow does not accumulate on the surface (Condition 1). In this case, the heat flux applied to the top surface of the deck is computed by multiplying the mass snowfall rate to the heat of fusion of snow. In addition, the convection and radiation losses still occur. If the transferred energy to the deck surface is enough to melt the falling snow, but the rate cannot match the snowfall rate, the falling snow does begin to accumulate on the surface (Condition 2). In this condition, the snow melting flux is defined by the sum of the conductive and latent heat fluxes. And if the transferred energy to the deck surface is not enough to melt the falling snow, the snow starts to cover the deck surface (Condition 3). In this case, the heat flux at the top surface is equal to zero indicating a Neumann boundary condition.

The process employed by Bowers (2016) for interpretation of the numerically obtained results when the snow melting flux equation was applied to the top surface of the deck model is shown in Figure 12. When the snow melting flux was applied, accumulated snow starts to melt in any portion of the deck with a surface temperature above freezing point. In locations with a surface temperature below 0 °C (32 °F), snow accumulation was expected. In this case, the model could be rerun assuming that the energy transfer rate was insufficient to melt any of the snow, and the boundary heat flux is zero. If the surface temperature of the deck remains below 0 °C (32 °F) under a Neumann boundary condition, Condition 3 exists and snow melting does not occur. A model with a surface temperature above 0 °C (32 °F) describes Condition 2. In this case, the system is melting the snow, but the deck is not 100 % clear of snow. This model results in an accurate response for temperature and energy values if Conditions 1 or 3 exist. When Condition 2 exists, temperature and energy results are accurate until the surface temperature drops below the freezing point. At this point, snow accumulation occurs and the actual heat flux will decrease towards 0 W/m^2. If the deck surface temperature is above 0 °C (32 °F) after applying the Neumann boundary condition, the system is still melting the snow, but at a rate less than the snowfall rate.

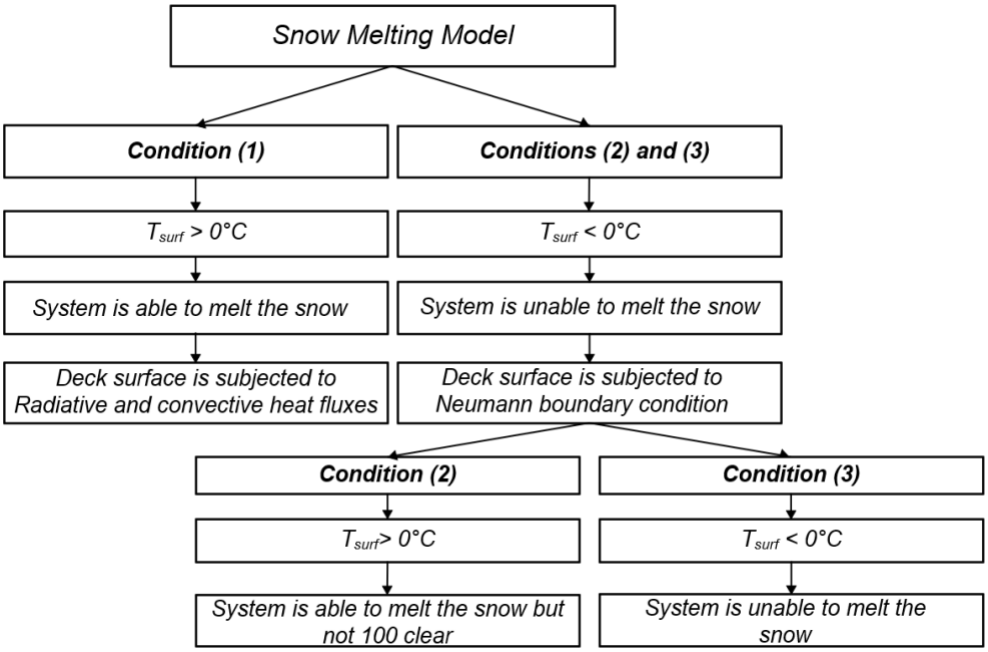

Figure 12. Interpretation of snow melting model proposed by Bowers (2016)

Boundary Conditions

The numerical model was developed with boundary and initial conditions, that matched the experimental setup by Bowers (2016). The initial condition for all domains in the numerical model was set according to the two weather conditions explained earlier. The top and bottom surfaces of the bridge deck model also had different boundary conditions according to the applied heating scenarios. In this section, the variables for each boundary condition that played an important role in the simulation process are described.

Thermal Radiation

In the case of thermal radiation from a bridge deck, two factors need to be specified: the surface emissivity constant (ε), and the external temperature (T_{ext}). Emissivity specifies the rate at which thermal radiation is emitted from a real surface as compared with emission from a black body at the same temperature (Howell et al., 2020). The emissivity range for concrete was found to be between 0.70 and 0.90 in the study conducted by Sen and Roesler (2019).

T_{ext} needs to be pre-computed and specified as a time-varying, or unsteady, parameter. Also, the external temperature is not necessarily equal to the ambient temperature (ASHRAE, 2013). According to ASHRAE (2013), the external temperature is equal to the mean radiant temperature (T_{MR}) which is defined as the equivalent black body temperature of the surroundings of the snow melting system. Different models have been proposed for mean radiant temperature (T_{MR}) (e.g., Ramsey et al., 1982; Martin and Berdahl 1984). The proposed model by Ramsey et al. (1982) is as Equation (12):

$$T_{MR} = [T_{cloud}^4 - F_{sc} + T_{sky\ clear}^4(1 - F_{sc})]^{1/4} \quad (11)$$

where F_{sc} is the cloud coverage, $T_{sky\ clear}$ is the equivalent blackbody temperature of the clear sky, and T_{cloud} is the cloud temperature. The variable $T_{sky\ clear}$ is obtained using Equation (13):

$$T_{skyclear} = T_a - [1.1058 \times 10^3 - 7.562(T_a) + 1.333 \times 10^{-2}(T_a)^2 - 31.292\emptyset + 14.58\emptyset^2] \quad (12)$$

where T_a is the ambient temperature (K) and $\emptyset$ is relative humidity of the air.

The part of the sky that is covered with clouds is assumed be at T_{cloud} (K), the temperature at the base of the clouds. The cloud base height is assumed to be 3048 m (10000 ft), and according to altitude, the temperature decreases 6.38k per 1000 m (3281 ft). Thus, the temperature of the clouds at 3048 m (10000 ft) is computed as Equation (14):

$$T_{cloud} = T_a - 19.4 \quad (13)$$

To estimate the sky temperature (T_{sky}) using Martin and Berdahl's (1984) model, a set of equations for monthly average clear sky emissivity ($\varepsilon_{skyclear}$), cloud emissivity (ε_{cloud}), and cloud factor (Γ_i) must be set. The monthly average clear sky emissivity ($\varepsilon_{skyclear}$) is calculated based on Equation (15):

$$\varepsilon_{skyclear} = 0.711 + 0.56\left(\frac{T_{dp}}{100}\right) + 0.73\left(\frac{T_{dp}}{100}\right)^2 + 0.013\cos\left[2\pi\frac{t_h}{24}\right] + 0.00012(P - 1000) \quad (14)$$

where T_{dp} is the dew point temperature, °F or ℃, t_h is the hour of the day, and P is the station pressure in millibar. The cloud emissivity (ε_{cloud}) is calculated by Equation (16):

$$\varepsilon_{cloud} = \varepsilon_{skyclear} + (1 - \varepsilon_{skyclear})\sum_i n_i \varepsilon_{c,i}\Gamma_i \quad (15)$$

where n_i is the fractional area of the sky covered at the i[th] level, $\varepsilon_{c,i}$ is the hemispherical emissivity of the cloud at the i[th] level, and Γ_i is the cloud factor at i[th] level. According to Bowers (2016), the low and mid-level clouds are generally opaque and have an emissivity value of 1, whereas the emissivity values for high-level clouds are around 0.4. The cloud factor (Γ_i) is defined by Equation (17):

$$\Gamma_i = e^{-h_i/h_o} \tag{16}$$

where h_i is the cloud base height, and $h_o$is the reference base height (8.2 km).

Finally, the sky temperature (T_{sky}) is calculated by Equation (18):

$$T_{sky} = T_a \cdot \varepsilon_{cloud}^{1/4} \tag{17}$$

Liu (2005) compared the results of the two models proposed by Ramsey et al. (1982) and Martin and Berdahl (1984) and indicated that the model proposed by Martin and Berdahl provided a better estimation of the sky temperature. According to AHRAE (1999), the prediction results by Ramsey et al. (1982) considerably underestimate the sky temperature when the relative humidity of air is very high.

Solar Radiation

The solar radiation from the sun can be calculated by determining the total direct incident radiation to a horizontal surface (I) and the solar absorptance (α). According to the sun's position in the sky throughout the year, the intensity of direct radiation on the surface can be determined. Equation (19) presents the formula that can be used for the estimation of solar radiation from the sun.

$$-n \cdot q = \alpha I \tag{18}$$

The direct component of the solar radiation can be calculated theoretically depending on the value of Air Mass (AM) at any position by Equation (20) (Duffie and Beckman, 1994):

$$I = 1.353 \times 0.7^{(AM^{0.678})} \tag{19}$$

where the Air Mass can be determined using the cosine of solar zenith angle (θ) (Equation (21)):

$$AM = \frac{1}{cos\theta} \tag{20}$$

The absorptivity coefficient (α) in the calculation of solar radiation depends on surface conditions. According to the study conducted by Levinson and Akbari (2001), the solar absorptance of concrete varies between 0.23 to 0.59. They also reported that the concrete has a maximum solar reflectance after a fresh snowfall.

Convection

As explained previously, there are two types of convective heat transfer mechanisms, forced convection, and free or natural convection. The effect of each case is tightly connected to the convective coefficient. According to the study conducted by Bergman et al. (2011), the range of

convective coefficients under free convection is much lower than forced convection. The influence of natural convection was accounted for the numerical model conducted by Liu (2005) when the wind was not present. Many laboratory experiments have been performed to determine the heat transfer coefficient due to natural or forced convection. In general, Equation (22) is used to compute the convection heat transfer coefficient (h_c) for the top and bottom of the bridge deck model:

$$h_c = N_u \frac{k_f}{L} \tag{21}$$

where the N_u is the Nusselt number, k_f is the thermal conductivity of the fluid, and L is the characteristic length. The characteristic length was defined as area divided by perimeter in the study conducted by Bejan (2013). As stated by Bowers (2016), as a conservative approach, the shortest dimension of the deck model can be selected as the characteristic length unless the air flow direction is known.

Incropera et al. (2006) presented Equation (23) for calculating the free convection heat transfer coefficient (h):

$$h=\begin{cases} \frac{k_a}{L}0.54Re_L^{1/4} & if\ T > T_{ext}\ and\ 10^4 \le Re_L \le 10^7 (laminar\ flow) \\ \frac{k_a}{L}0.15Re_L^{1/3} & if\ T > T_{ext}\ and\ 10^7 \le Re_L \le 10^{11} (turbulent\ flow) \\ \frac{k_a}{L}0.27Re_L^{1/4} & if\ T \le T_{ext}\ and\ 10^5 \le Re_L \le 10^{10} (turbulent\ flow) \end{cases} \tag{22}$$

where the Re_L is the Reynolds number.

The average convective heat transfer coefficient for external forced convection on a horizontal surface can be computed by Equation (24) (Welty et al., 2014):

$$h=\begin{cases} 2\frac{k_a}{L}\frac{0.338\,P_r^{1/3}Re_L^{1/2}}{(1+(\frac{0.0468}{Pr})^{2/3})^{1/4}} & if\ \ Re_L \le 5\times10^5\ (laminar\ flow) \\ 2\frac{k_a}{L}\,P_r^{1/3}\,(0.037Re_L^{\frac{4}{5}} - 871) & if\ \ Re_L > 5\times10^5 (turbulent\ flow) \end{cases} \tag{23}$$

where P_r is the Prandtl number of air which according to ASHRAE (2013) can be considered to be 0.7.

Model Development

A series of 3D numerical simulations of a bridge deck deicing system were performed using the finite element software COMSOL Multiphysics. The experiments conducted by Bowers (2016) was used for model validation. Several components of the bridge deck deicing system, including the circulating fluid, heat exchanger pipes, and concrete deck were included in the numerical model. In this study, 1D linear elements were employed to model fluid flow and heat transfer inside the heat exchanger pipes. The flow rate, pressure, and temperature were modeled as the average cross-section quantities, so they only vary along the length of the pipes. The pipeline

pressure loss was defined using friction factors. The thickness and thermal conductivity of pipe wall were assigned by adding external wall resistance.

Model Geometry and Material Properties

The configuration of the baseline model and meshed model of the bridge deck is shown in Figure 13(a) and (b), respectively. The geometric dimensions and material properties adopted in the numerical simulation are listed in Table 11. The material properties used in this study were taken from the numerical study conducted by Bowers (2016). The heat exchanger pipes were modeled using 1D linear elements. Non-isothermal flow and heat transfer in solids modulus were employed in numerical modeling. The rebar was not modeled in the numerical analyses; but, to account for the respective volumetric percentages of rebar in each zone, the concrete deck was divided into three zones. In the experimental model, the top and bottom zone included rebar reinforcement, and the middle zone included pure concrete. In this regard, the material properties assigned to each domain were based on a volumetric average of concrete and rebar, as presented in Table 11.

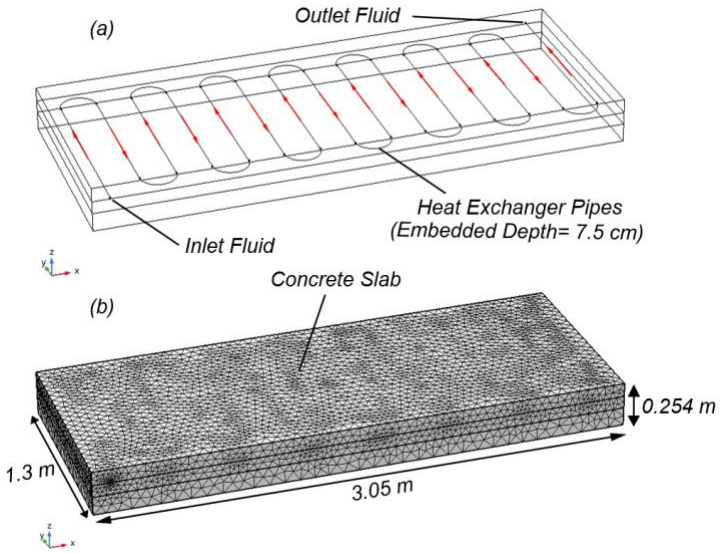

Figure 13. (a) The bridge deck model configuration, (b) Meshed 3D model

Model Validation

Two experimental test conditions were selected for model validation based on their ability to isolate and assess certain boundary conditions: 1) a bridge deck with accumulated snow on the surface, and 2) a bridge deck during a period of cold weather (with no snow on the surface) followed by snowfall. Snow has an extremely low thermal conductivity and is a very good insulator. In the first bridge deck model, both top and side surfaces of the deck were insulated. This model was used to explore the effect of material properties and the surface boundary condition on the heating process of the deck. The snow melting process of accumulated snow was not considered in this series of analyses. The second model was used to 1) test the boundary conditions of the model as the deck was clear during the initial part of the test and subject to radiation and convection with the environment, and 2) test the snowmelt model as the snow is falling.

First Scenario- Severe Winter Event

The accuracy of the numerical model was verified with the corresponding measured data during the severe winter event. As presented earlier, almost 20 cm of snow accumulated on the surface during this cold event. The top surface boundary condition and the edges of the bridge deck model was insulated (no heat flow) due to snow insulating effect. A Neumann condition was applied to the top and edges of the bridge deck model. In addition, the bottom surface was subjected to the thermal radiation employing the ambient air temperature.

Table 11. List of the material properties of the experimental and numerical models (Bowers, 2016)

Parameter	***Experimental***	***Numerical***
Bridge Deck Dimensions		
Length (m)	3.0	3.0
Width (m)	1.3	1.3
Height (cm)	25.4	25.4
Depth of circulation pipes (cm)	7.4	7.4
Circulation Fluid (20% Glycole)		
Flow rate (L/m)	15.1	15.1
Dyncamic Viscosity (mPa.s)	4.8	4.8
Thermal conductivity (W/m.k)	0.4	0.4
Specific heat capacity (J/kg.k)	3538.0	3538.0
Density (Kg/m^3)	1070.0	1070.0
Concrete		
Thermal conductivity (W/m.k)	3.0	3.0
Specific heat capacity (J/kg.k)	880.0	880.0
Density (Kg/m^3)	2360.0	2360.0
Concrete/Rebar Zones		
Top height (cm)	-	7.40
Bottom height (cm)	-	10.20
Top thermal conductivity (W/m.k)	-	3.65
Top specific heat capacity (J/kg.k)	-	873.82
Top density (Kg/m^3)	-	2443.80
Bottom thermal conductivity (W/m.k)	-	3.48
Bottom specific heat capacity (J/kg.k)	-	875.42
Bottom density (Kg/m^3)	-	2422.10

Figure 14 compares the measured and predicted variation of the inlet and outlet fluid temperatures during system operation. The temperature change in the numerical investigation matched well with Bowers (2016) experimental tests. The difference between inlet and outlet fluid temperature reflects the absorbing heat ability. In fact, the amount of energy added to the deck can be computed by multiplying the density of circulating fluid by the specific heat capacity of circulating fluid by the volumetric flow rate circulating fluid and the temperature difference of fluid between the inlet and outlet. As shown, the difference between the inlet and outlet fluid temperature decreased with time indicating that the energy added to the deck decreased as well. The maximum and minimum difference between the inlet and outlet fluid temperature was 2.08 °C (35.7 °F) and 0.33 °C (32.6 °F), respectively. The largest discrepancy between the predicted and measured values was

observed between minutes 10 and 80 which could be associated with the uncertainties in selected material properties, (e.g., volumetric average of concrete and rebar), and bottom surface boundary condition.

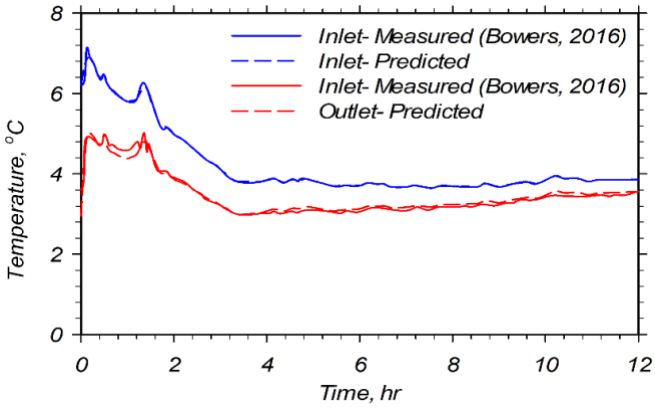

Figure 14. Experimentally recorded and predicted time histories of inlet and outlet fluid temperature

Figure 15 compares the variation of measured and predicted temperature at different locations along two cross-sections in the middle of bridge deck. The results of the measured temperature corresponds to the thermal sensors located at a cross section with a heat exchanger pipe (Figure 15(a)) and a cross-section without a heat exchanger pipe (Figure 15(b)). The simulation results agreed well with the test results. It was important for the predicted top surface temperature to be in good agreement with the measured values since the failure or success of the system could be judged through this observation (Bowers, 2016). The results indicated that the top surface temperature was higher at the location above the heat exchanger pipe as compared to the location between the pipes during the whole system operation. In addition, the temperature change rate was higher during the initial hours. This is because there were higher ambient temperature and inlet fluid temperature during these hours.

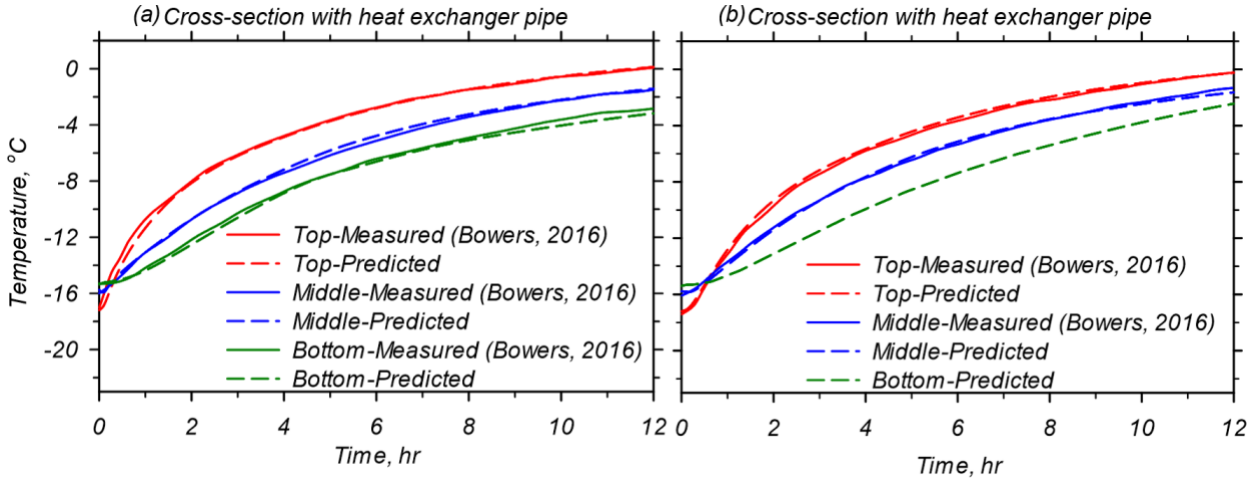

Figure 15. Comparison between experimental results and numerically predicted values of temperature at the top, middle, and bottom location within the bridge deck at (a) cross-section with heat exchanger pipes, (b) cross-section without heat exchanger pipes

Figure 16 displays the cross-sectional and top surface temperature contours at different times of simulation. At the start of heating, the cross-sectional and top surface temperature distribution was relatively uniform between -15 °C (5 °F) and -17 °C (1.4 °F) (Figure 16a). After 4 hours of heating, the surface temperature above and between the heat exchanger pipes was increased to the average of -4.8 °C (23.4 °F) and -5.9 °C (21.4 °F), respectively. The temperature distribution within the deck illustrated a large temperature gradient at this time (Figure 16b). The temperature along the cross-section varied between -3 °C (26.6 °F) to -10 °C (14 °F). The maximum temperature within the deck appeared around the heat exchanger pipes while the minimum temperature appeared at the bottom deck surface. After the deck was heated for 8 hours, the surface temperature distribution became relatively uniform at -2 °C (28.4 °F) (Figure 16c). A temperature range of -1 °C (30.2 °F) to -5.8 °C (21.6 °F) was observed within the deck model. Like the simulation results observed after 4 hours of heating, the temperature of the deck near the heat exchanger pipes was higher and the coldest region within the deck was observed at the deck bottom. The results indicated that it took 12 hours for average deck surface temperature to reach the freezing point (Figure 16d). The deck bottom still had the lowest temperature compared to other regions within the deck. Also, the smallest temperature gradient of around 3 °C (37.4 °F) was seen at this time.

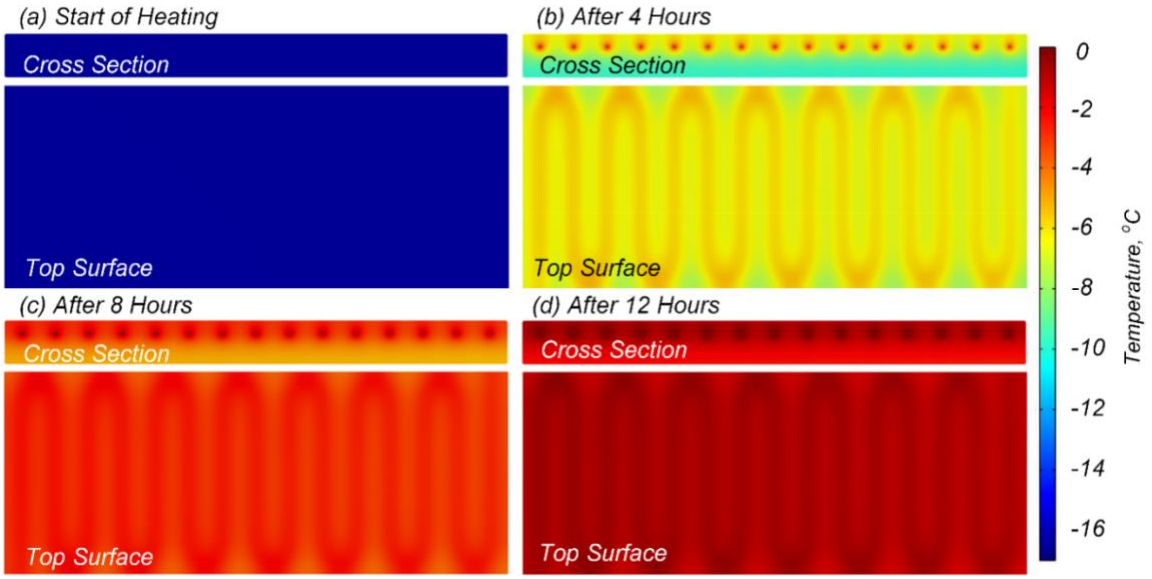

Figure 16. The progression of the cross-sectional temperature and the top surface temperature over time obtained in this study

Second Scenario- Moderate Winter Event

Validation of the model was conducted using the experimental test conducted by Bowers (2016) during the moderate winter event recorded on February 25-26, 2015. As described earlier, 7.6 cm (3 inch) of snow fell over approximately 5 hours. A variety of weather conditions were considered in the numerical modelling, including sunny, partially cloudy, cloudy, and snowy weather. The top surface of the bridge deck model was subjected to both convective and radiative heat fluxes since the system was not covered with snow at the beginning of the operation. In addition, a Neumann condition was applied to the edges of the bridge deck model. Heat transfer on the bottom

surface of the deck model was by means of natural convection and radiation. For the radiant and natural convective boundary conditions, the external temperature of the top and bottom surfaces was taken as T_{sky} and ambient temperature, respectively. Figure 17 shows the unsteady values input to the numerical model, including ambient temperature, sky temperature, solar radiation and snow melt flux.

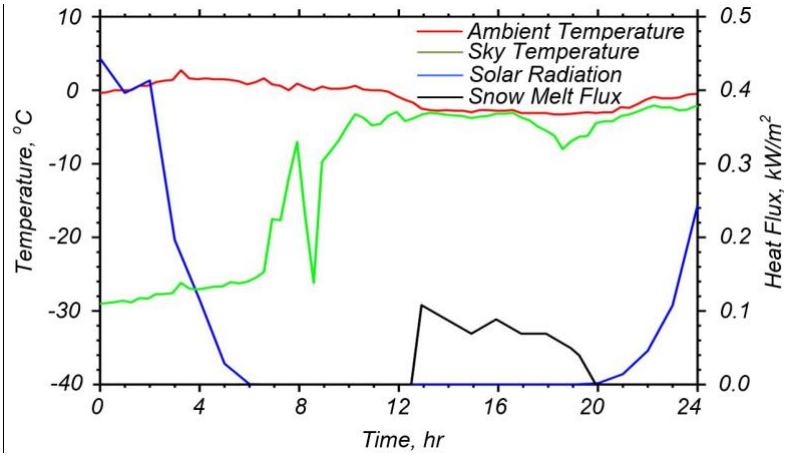

Figure 17. Variation of ambient and sky temperature during the experimental test and input heat fluxes to the numerical model (Bowers, 2016)

The predicted and measured inlet and outlet fluid temperatures are compared in Figure 18. As stated earlier, the difference between the inlet and outlet temperatures of the heating fluid plays an important role in the analysis of the energy required for snow melting. The experimental results indicated that there was a considerable difference between the measured inlet and outlet fluid temperatures after 4 hours of system operation compared to those predicted numerically. Thereafter, the measured temperature difference considerably decreased. Based on the conservation of energy, a lower heating rate to the deck can be expected during this time. As shown in Figure 18, there was a considerable difference between the measured and predicted outlet temperatures. This observation was also reported by Bowers (2016) and attributed to errors in weather parameters, boundary conditions, and material property uncertainties. The results also indicated that the temperature difference as well as the corresponding imparted energy to the deck surface increased when the snow melting heat flux method was applied to the system (hours 12.5 to 20) and started to decrease when the deck surface was free from snow (hours 12 to 24). The predicted temperature change agreed well to the laboratory experiments during these time periods.

Figure 19 illustrates the measured and predicted temperature variation over time at different locations along a cross-section in the middle of the bridge deck, which included a heat exchanger pipe. The results for a cross-section between heat exchanger pipes is shown in Figure 20. The measurement points were shown in Figure 7(b). Temperature changes in the numerical investigation were close to the experimental results. The highest surface temperature was recorded during the daytime after 2.5 hours of system operation. This observation could be associated with the effects of high inlet fluid temperature, as shown in Figure 18, and the existence of solar radiation from sun, as shown in Figure 17. The largest discrepancy between the predicted and

measured values was observed between 4 and 12 hours of operation. The difference between the predicted and observed values most likely results from using the mean ambient temperature as the sky temperature in the numerical simulation. As reported by Bowers (2016), there was a maintenance shed on one side of the deck, a mound of soil on the other side, and nearby buildings and trees about 7 m (23 ft) from the deck. Considering the effect of these surroundings, T_{MR} could be different than T_{sky}. In addition, the thermal conductivity of the concrete and specific heat capacity were not measured experimentally by Bowers (2016). It was reported in many previous studies (e.g., Liu, 2005) that the deck surface temperature was sensitive to the thermal properties of the deck material. According to Kim et al. (2003), the thermal conductivity of concrete was strongly affected by type of admixture, density, and humidity condition of concrete. Therefore, the suggested concrete material properties by Bowers (2016), which were used in the numerical simulation, could result in some error. Furthermore, as explained earlier, the rebar was not modeled in the numerical analyses, and the material properties of each domain were assigned based on a volumetric average of concrete and rebar. This simplification could also lead to some errors. Weather data was another uncertainty that was reported by Bowers (2016). As reported, two sources were used to collect weather data: 1) a weather station at Virginia Tech Airport, located about 6.76 km (4.2 miles) from the project site, and 2) a weather station at Kentland Farm, located 4 miles from the project site in the opposite direction. The weather data was reported by the Virginia Tech Airport station every 20 min and once an hour by the other station. The sky temperature was calculated using the data provided by the Virginia Tech Airport station due to a higher frequency of data. The solar radiation and precipitation amounts were computed using the data from the weather station at Kentland Farm. As reported by Bowers (2016), the collected weather data may not be representative of the project site weather due to the distance from the project site. Therefore, the predicted weather data, especially the sky temperature, which can vary based on the hourly values of cloud cover, could be considered as one possible source of error in the numerical simulation. The results also delineated that the predicted values matched better with the measured values between the hours of 12 and 24, as the sky temperature was getting close to the ambient temperature due to cloud coverage. A similar trend was observed in the different locations within the deck, as shown in Figure 19 and Figure 20 (b), (c), and (d).

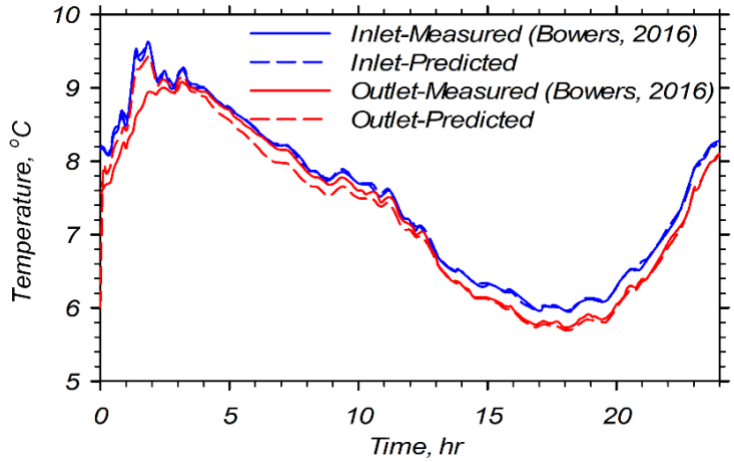

Figure 18. Experimentally recorded and predicted time histories of inlet and outlet fluid temperature

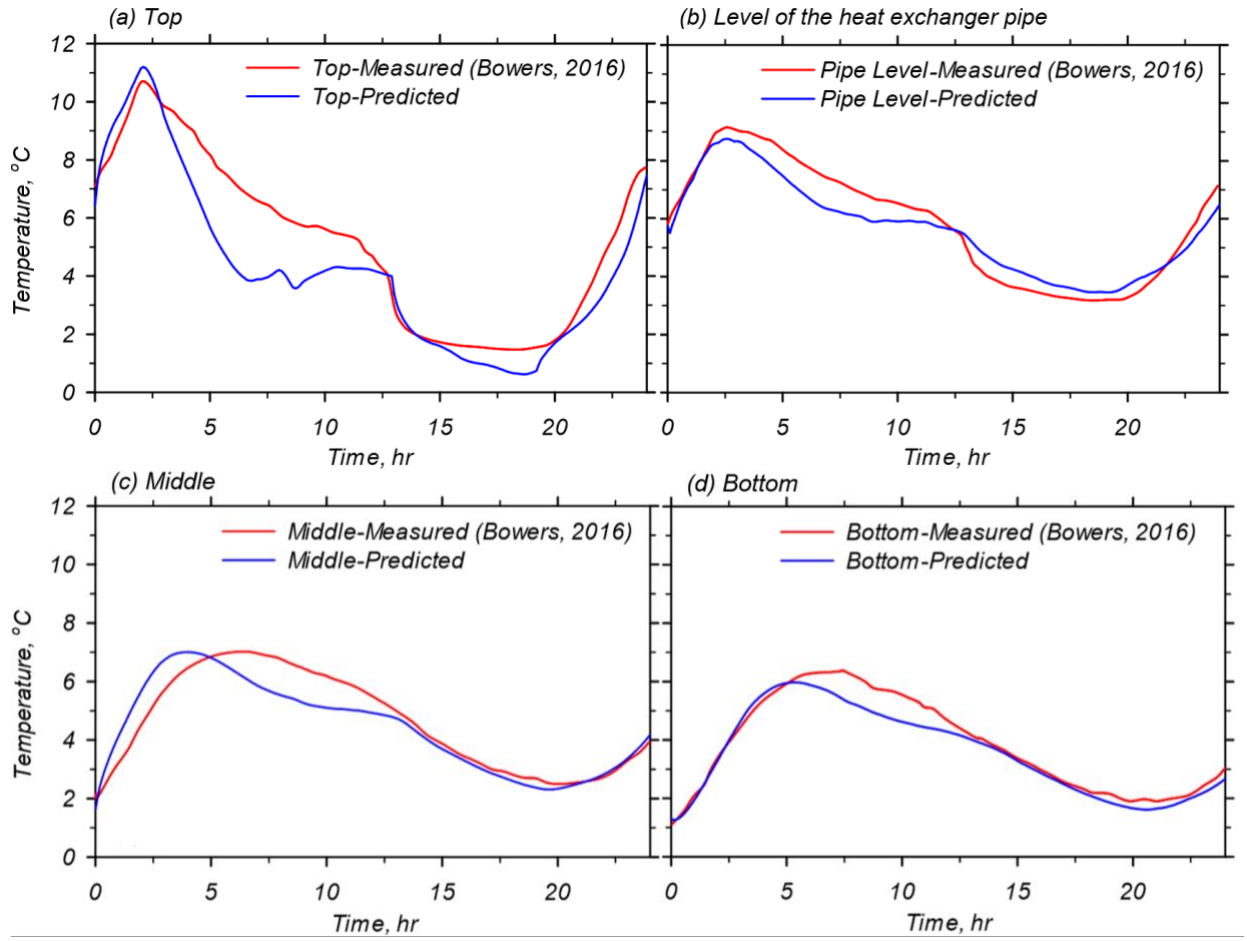

Figure 19. Comparison between experimental results and numerically predicted values of temperature at the top, pipes, middle, and bottom locations within the deck at cross-section with heat exchanger pipes

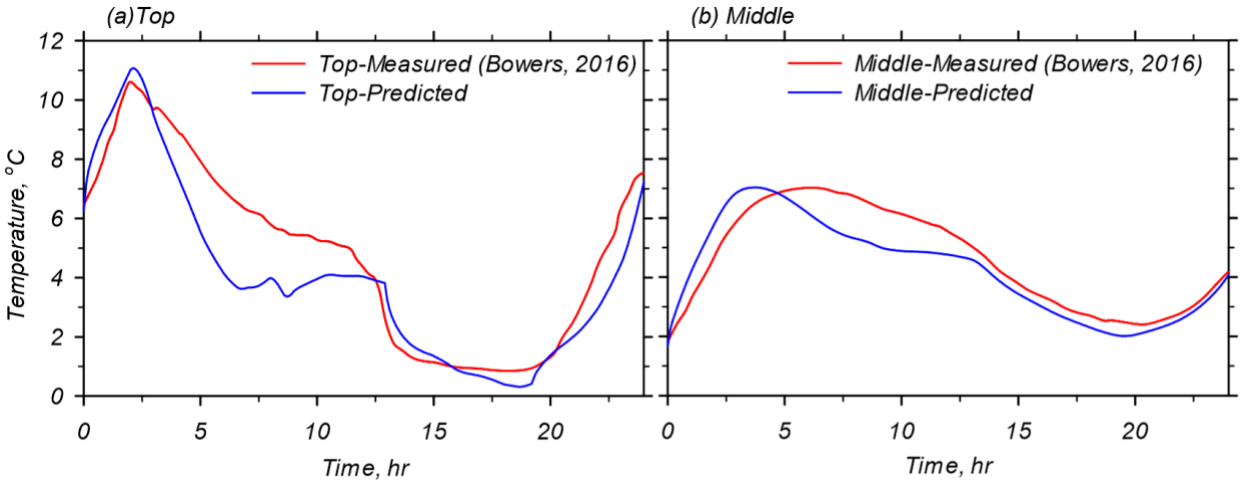

Figure 20. Comparison between experimental results and numerically predicted values of temperature at the top and middle locations within the deck at cross-section without heat exchanger pipes

Figure 21 illustrates the top surface and cross-sectional temperature distribution over time. The top surface temperature had a uniform value of 6.7 °C (44.1 °F) when the system was turned on (initial condition). In addition, there was an initial temperature gradient in the deck model (Figure 21a). After the deck was heated for 3 hours, the top surface temperature reached a uniform value of 9.5 °C (49.1 °F) (Figure 21b). The temperature contours show that the top surface experienced higher temperatures compared to other parts of the bridge deck model during the day. As stated earlier, this could be attributed to the higher inlet fluid temperature and top surface exposure to sun. After 12 hours of heating, right before the storm event, the deck surface temperature increased to an average of 4.25 °C (39.65 °F) (Figure 21c). The region around the heat exchanger pipes had the highest temperature and the average temperatures of top and bottom surfaces were lower than other regions within the deck model. Based on the temperature contours, the top surface temperature was still above the freezing point (0 °C (32 °F)) after 16 hours of simulation (Figure 21d). As expected, the top surface had the lowest temperature as the snowmelt heat flux was applied for deicing.

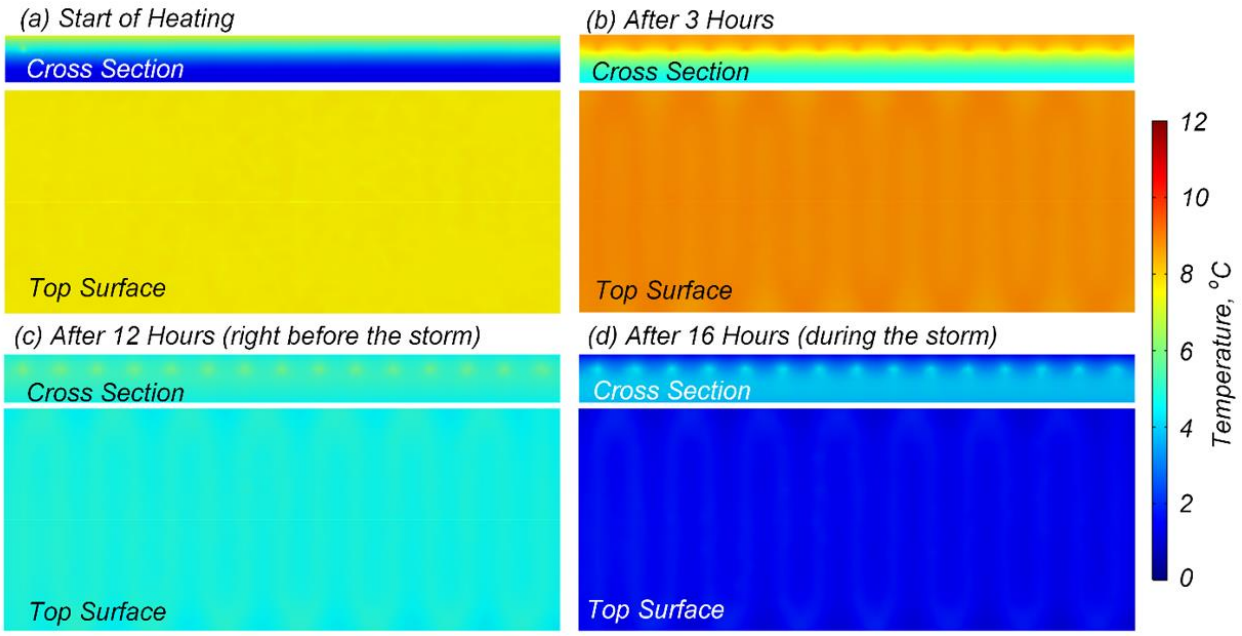

Figure 21. Progression of the cross-sectional temperature and top surface temperature over time obtained in this study

Conclusion

Through the comparison of modeled and experimental results, it can be concluded that:1) the material properties employed in the numerical model were representative of those in the field, 2) modification of the thermal conductivity of concrete based on the respective volumetric percentages of rebar in each zone could be used in the simulation process as the predicted values matched the actual values, and 3) the validated model could be used to predict the temperature distribution and propagation within the deck for any similar boundary conditions.

CHAPTER 5: NUMERICAL STUDY OF BRIDGE DECK DEICING IN MONATANA STATE

Introduction

In this chapter, the validated numerical model was employed to evaluate the performance and feasibility of bridge deck deicing using geothermal energy for Montana weather conditions. Climate conditions are the most significant variables in designing a bridge deck deicing system. The weather data from the sites in Montana where icing and maintenance are known to be a problem are incorporated for investigation. As reported in the previous task report, the Road Weather Information System (RWIS) has been adopted by many state transportation agencies, including MDT. There are 73 RWIS stations in the state of Montana. Each of these 73 stations includes an air temperature and humidity sensor, wind speed and direction sensor, in-pavement temperature sensor, subsurface temperature sensor, precipitation sensor, and a camera. Six sites (or fewer) are also equipped with advanced precipitation sensors, visibility sensors, or infrared illuminators for nighttime camera images (Al-Kaisy & Ewan, 2017).

Montana Weather

In Task Report 1, the time histories of weather data, including ambient temperature, pavement surface temperature, sub-surface temperature, relative humidity, wind speed, and average snowfall accumulation over the period of 2015 to 2020, were collected from 73 RWIS stations. The results indicated that climate conditions specifically for the months of November through February of the next year must be considered for designing a bridge deck snow melting/deicing system for the state of Montana. These winter months typically had the heaviest snowfall and the lowest ambient temperature. Representative examples of weather data recorded at the Lookout Pass station near Missoula from 2015 to 2020 are shown in Figure 22. Table 12 presents important weather parameters for the selected winter events recorded in Montana. The inlet fluid temperature range considered in the numerical simulations is also shown in Table 12.

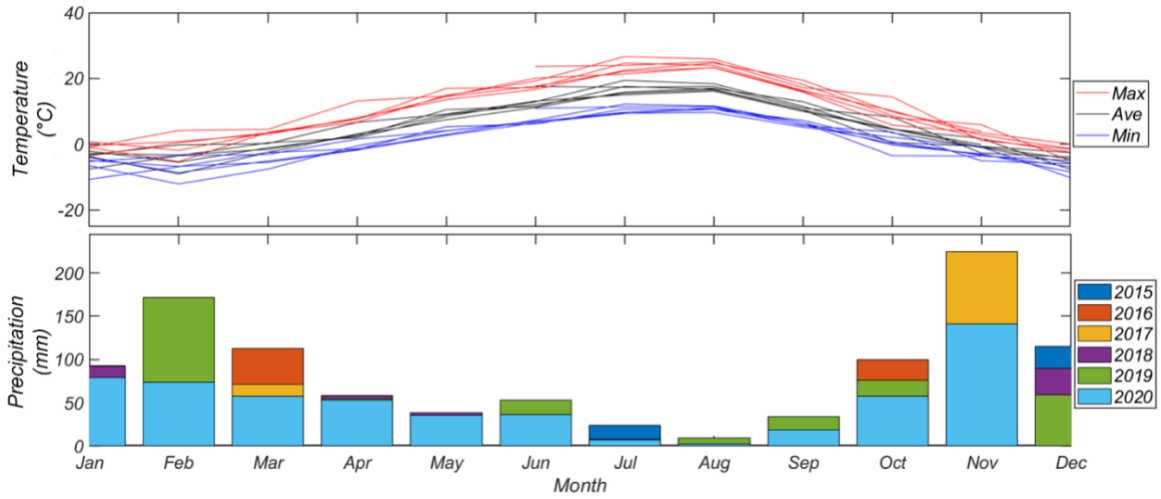

Figure 22. Monthly average weather data for 2015-2020: (a) ambient temperature, and (b) precipitation

Table 12. Selected weather parameters and experimental test results of snow melting

Cold event (time)	***Severe winter event (23-24 January 2019)***	***Moderate winter event (11-13 February 2019)***
Ambient temperature (°C)	-2 to -17 (28.4 °F to 1.4 °F)	-3 to -8 (26.6 °F to 17.6 °F)
Depth of snow (cm)	28 (11 inches)	7 (2.75 inches)
Starting time of operation	15:00, 1/23/2019	In operation
Circulating fluid temperature (°C)	6.1 (43.0 °F)	8.0 (46.4 °F)

As previous studies showed (e.g., Kusuda & Achenbach, 1965), seasonal variation of ground temperature is minimal at a depth approximately 6-9 m (20-30 ft) below the ground surface. Based on the earth temperature contours across the US, the mean earth temperature in Montana ranges from a low of 6.1 °C (43 °F) in the east to a high of 10.0 °C (50 °F) in the south.

First Scenario- Severe Winter Event- Great Falls, January 23-24, 2019

The validated numerical model was first used to evaluate the feasibility of a bridge deck snow melting/deicing system for a severe winter event recorded in Great Falls, Montana. Figure 23 illustrates the time histories of the ambient temperature and cumulative snowfall on January 23-24, 2019. The data indicates that the 28 cm (11 ft) of snow accumulated over the course of 10 hours on January 23, 2021. The ambient temperature during the snowfall varied between -2 °C (28.4 °F) to -17 °C (1.4 °F). In this scenario, it is assumed that the system was not turned on before the storm; thus, the bridge deck was covered with snow. The starting time of heating was assumed to be at 15:00 on January 23, 2019. The snow melting process was not considered in these analyses, however, the ability of the system to keep the temperature of the bridge deck above freezing was studied. It was assumed that the accumulated snow acted as an insulator to the top surface of the bridge deck; therefore, the top surface was not subjected to the radiative and convective heat fluxes.

Figure 24 illustrates the predicted temperature at different locations within the deck model for a cross-section including a heat exchanger pipe (Figure 24a) and for a cross-section between heat exchanger pipes (Figure 24b). The initial temperature within the deck was assumed to be equal to the ambient temperature before the storm event (-4 °C (24.8 °F)). The results indicated that the temperature within the deck was increasing during the storm despite a decrease in ambient temperature. It should be noted that the system was able to heat the deck surface to above freezing after 3 hours of simulation according to the model. After that, the top surface temperature remained above the freezing point even though the ambient temperature dropped to -18 °C (-0.4 °F).

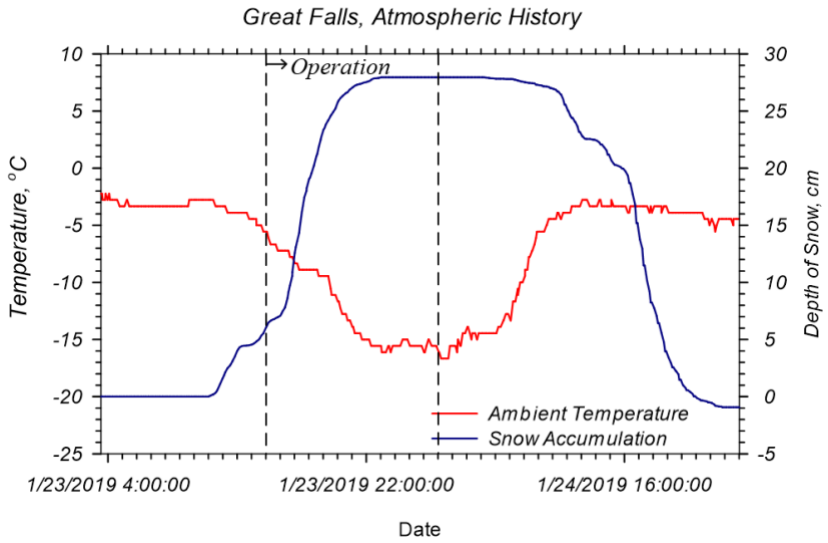

Figure 23. Atmospheric history of Great Falls, MT, on January 23-24, 2019.

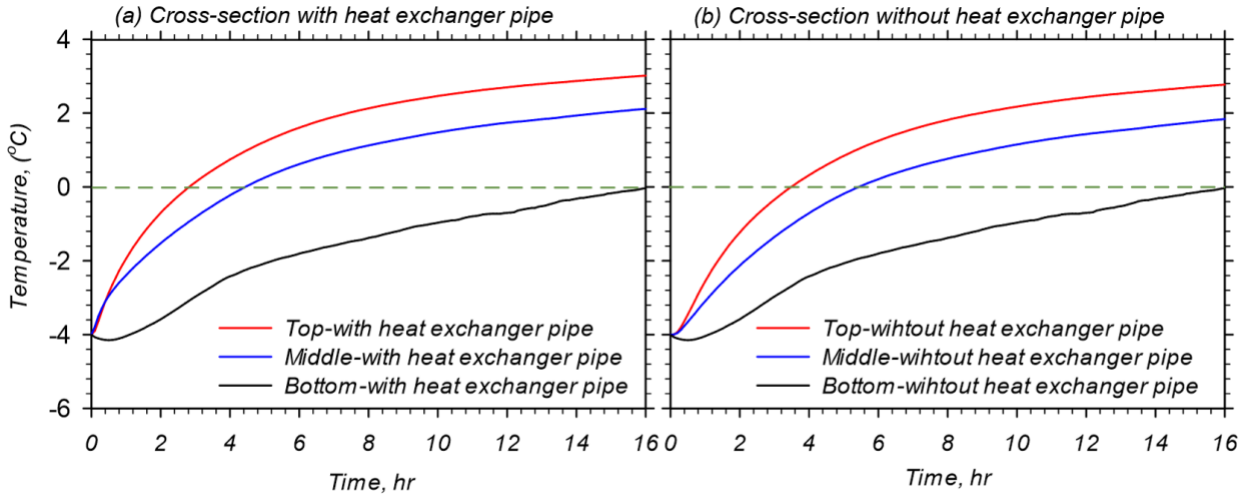

Figure 24. Predicted temperature at different locations within the bridge deck model for a (a) cross-section without heat exchanger pipe, (b) cross-section including a heat exchanger pipe.

The bridge deck cross-sectional and top surface temperature contours at different times are shown in Figure 25. The results indicated that after 3 hours of system operation, the system was able to increase the top surface temperature above the freezing point (Figure 25b). It was seen that the regions above the heat exchanger pipes had higher temperatures compared to the regions between the pipes. It was also noted that the warmest and coldest regions of the bridge deck model were around the heat exchanger pipes and the bottom surface, respectively. After 10 hours, the top surface temperature ranged between 2.2 °C (36.0 °F) and 2.4 °C (36.3 °F) (Figure 25c). Additionally, it was found that the average bottom surface temperature was -1 °C (30.2 °F). After 16 hours of simulation, the average top surface temperature was 2.8 °C (37.0 °F) (Figure 25d). The temperature contour results also showed that the entire deck was above freezing at this time.

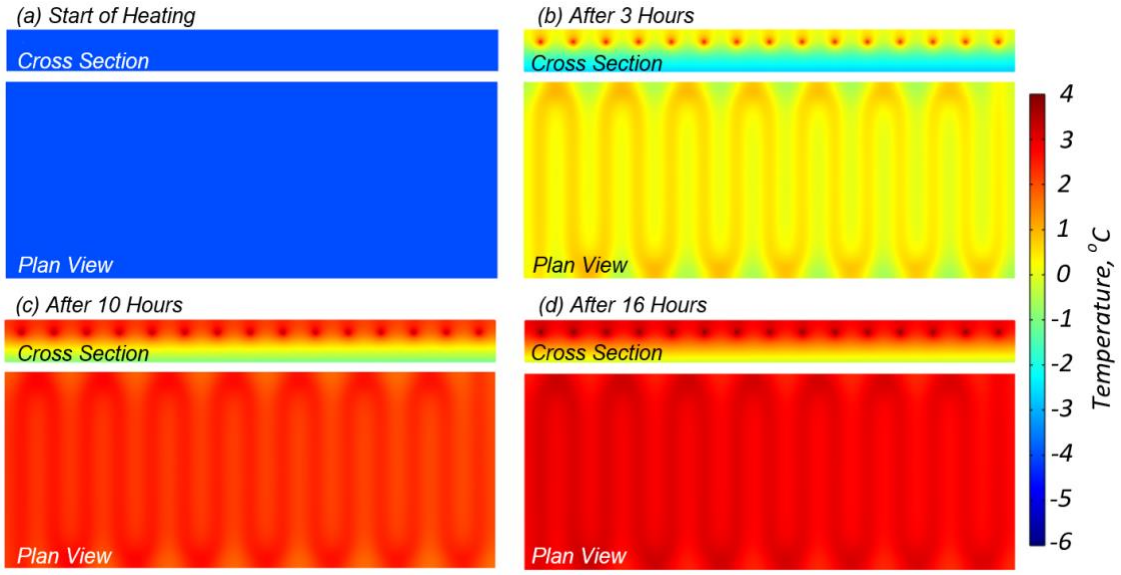

Figure 25. Top surface temperature and temperature distribution along the cross-section in the middle of bridge deck model at different simulation times.

Second Scenario- Moderate Winter Event- Missoula, Lookout Pass, February 11-13, 2019

The validated numerical model was then used to study the performance of the bridge deck deicing system during a cold weather event combined with 7 cm of snowfall. Figure 26 shows the ambient temperature and cumulative snowfall recorded in Missoula, Montana. The snowfall began on February 11, 2019, around 22:00 and continued until February 13, 2019, 6:00. The recorded data indicated that the snow had accumulated with a higher rate between the hours of 7:00 and 17:00 on February 12, 2019. The ambient temperature varied between -2 °C (28.4 °F) and -9 °C (15.8 °F) during the storm. Unlike the previous scenario, it was assumed that the heating system was in operation at the beginning of the storm. Preliminary results suggested that a minimum inlet fluid temperature of 8 °C (46.4 °F) was required to maintain the deck surface temperature above freezing (0 °C (32 °F)) during the storm. The initial temperature of the top, middle, and bottom portion of the bridge deck was set at 7.0 °C (44.6 °F), 2.4 °C (36.3 °F), and 1.2 °C (34.2 °F), respectively. The temperature gradient along the deck depth was obtained based on the results of the model validation.

Figure 27 lists the input variables to the numerical model for the second weather event. Since sky temperature (T_{sky}) was not included in the RWIS, the model proposed by Martin and Berdahl (1984) was adopted to compute T_{sky}. As presented in the previous chapter, to compute T_{sky}, dew point, station pressure, and cloud coverage, were required. The dew point and station pressure were taken from RWIS, and the cloud cover information was gathered from the available online resources (e.g., Time and Date website at https://www.timeanddate.com). The incident solar radiation during the event is also shown in Figure 27. The solar zenith angle (θ) for computing solar radiation from the sun was obtained from National Oceanic and Atmospheric Administration (NOAA). The incident solar radiation during snowfall was not considered in this simulation. This assumption should result in a more conservative response.

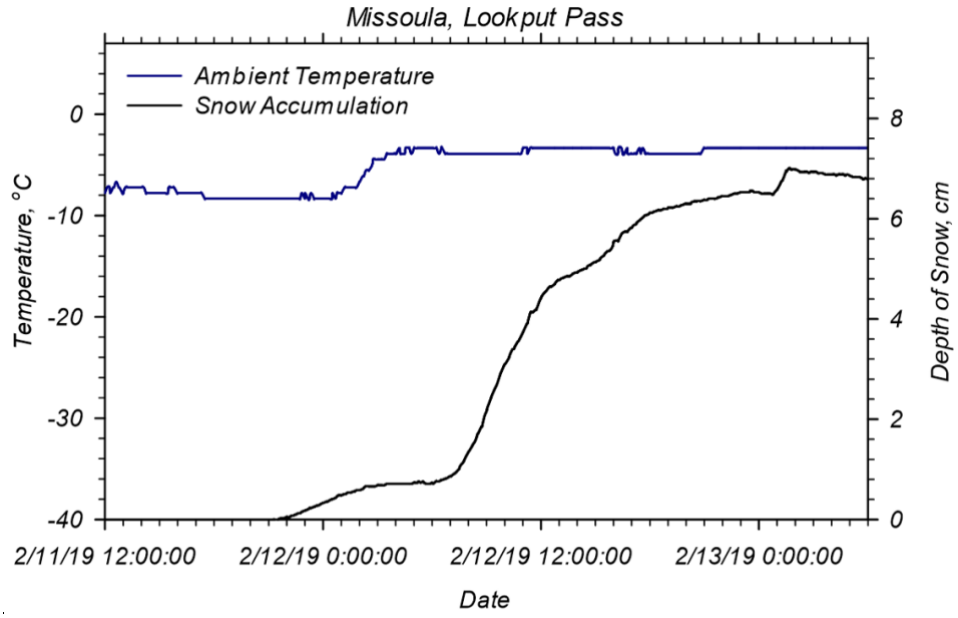

Figure 26. Atmospheric history of Lookout Pass, Missoula, MT, on February 11-13, 2019.

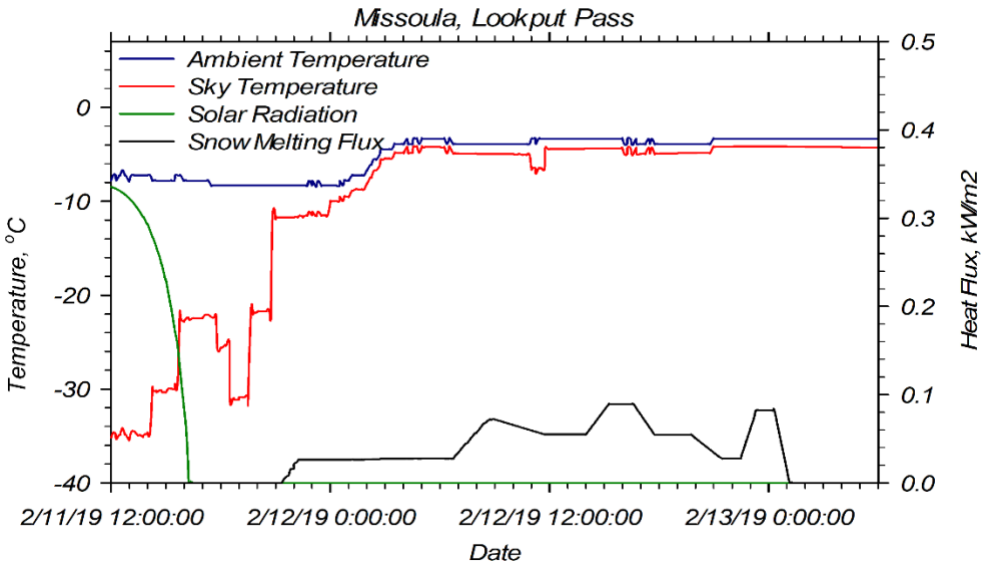

Figure 27. Applied condition to the numerical model in the second simulation.

Figure 28 shows the variation of temperature at different locations within the bridge deck model. The highest deck surface temperature was observed between 0 and 4 hours, when the top surface was exposed to solar radiation from the sun. Then, the temperature at different locations within the deck model decreased as the incident solar radiation decreased. When the snow began to fall, the deck surface temperature was above freezing (0 °C (32 °F)) and remained above 0 °C (32 °F) during the entire weather event despite below freezing ambient temperatures. It should also be noted that the highest temperature for this simulation occurred within the deck around the heat exchanger pipes nearest to the heat source.

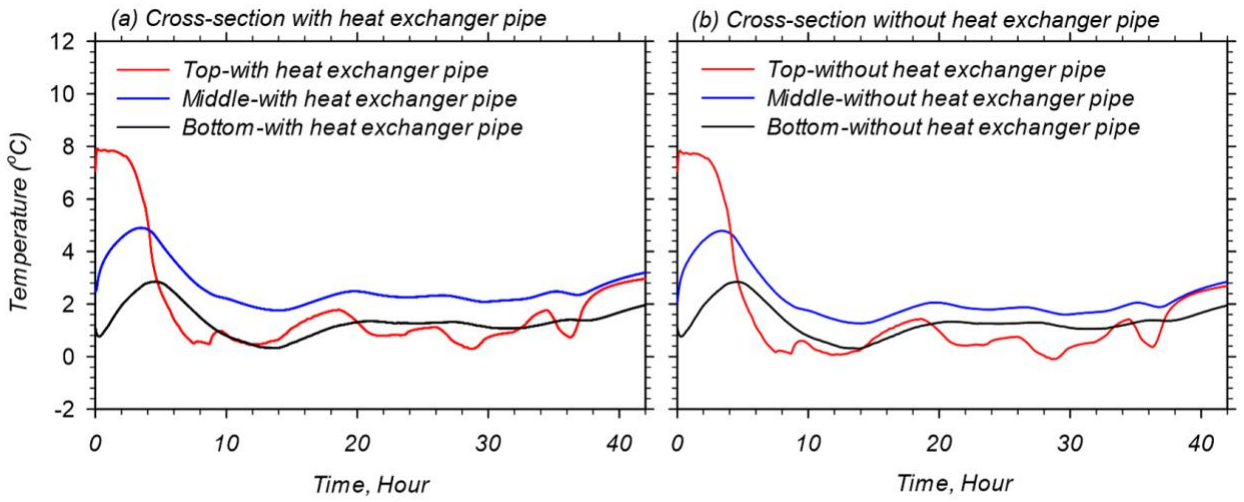

Figure 28. Predicted temperatures at different locations within the bridge deck model for (a) a cross-section without heat exchanger pipe, and (b) a cross-section including a heat exchanger pipe

Figure 29 displays the predicted cross-sectional and top surface temperatures of the bridge deck model at different simulation times. As stated before, a preexisting temperature gradient was applied to the interior of the deck model (Figure 29a). After 4 hours of simulation, the highest temperature was observed at the top surface (Figure 29b). Thereafter, the deck began to lose energy to the environment when solar radiation ceased. As a result, the temperature within the deck dropped almost uniformly between 0 °C (32 °F) and 2 °C (35.6 °F) (Figure 29c). The results indicated that the heating system could maintain the temperature above freezing within the deck model during the entire winter event, especially the top surface temperature (Figure 29d). After 42 hours of simulation, the system was able to increase the top surface temperature to an average of 2.8 °C (37.0 °F) (Figure 29e).

Discussion and Conclusion

A numerical simulation was used to evaluate the performance of a specific snow-melting system during two different winter weather conditions in Montana. Two major assumptions were made to assess the performance of the heating system during different weather conditions. During the severe winter event, it was assumed that the system was non-operational before the snowfall, and snow accumulated on the surface. The initial deck surface temperature was assumed to be equal to the ambient temperature before the storm event (-4 °C (24.8 °F). During the moderate winter event, the system was assumed to be in operation in anticipation of the storm event and the average top surface temperature reached to a temperature as high as 7 °C (44.6 °F).

During a severe winter event, a bridge deck deicing system with a tube spacing of 20 cm and an inlet fluid temperature of 6.1 °C (43.0 °F) could increase the bridge deck surface temperature above the freezing point after 3 hours. The system could maintain the bridge deck surface temperature above 0 °C even though the ambient temperature severely dropped. For a moderate winter event in Montana, the model results indicated that a bridge deck deicing system with a tube spacing of 20 cm and an inlet fluid temperature of 8 °C (46.4 °F) was able to keep the surface

temperature above the freezing point providing that the bridge deck was preheated to 7 °C (44.6 °F) before the snowfall. Therefore, snow accumulation would not be expected during the storm.

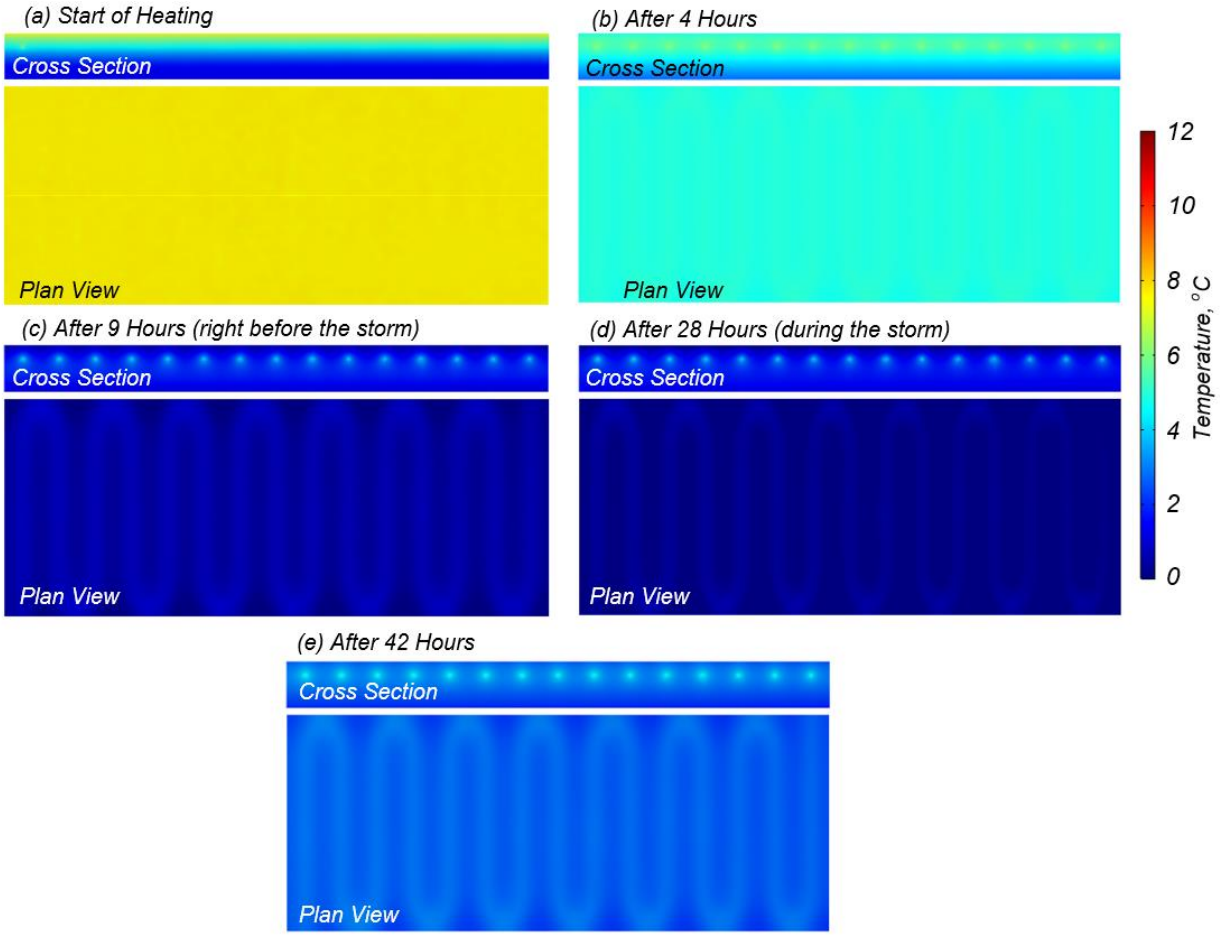

Figure 29. Cross-sectional and top surface temperature of the bridge deck model during the cold weather event.

Additional analyses for different system configurations and different Montana weather conditions such as a change in the inlet fluid temperature, inlet fluid rate, tube spacing, top and bottom reinforcement cover, ambient temperature, wind speed, and snowfall rate which are not reported in this task report will be performed in future to examine the influence of each parameter on the performance of the snow melting/deicing system. The finding from the analyses can serve as a practical solution for designing a bridge deck deicing system.

REFERENCES

Al-Kaisy, A., & Ewan, L. (2017). Prioritization scheme for proposed road weather information system sites: Montana case study. *Frontiers in built environment, 3*, 45.

American Society of Heating Refrigerating and Air-Conditioning Engineers (ASHRAE) (1999). ASHRAE Handbook - Fundamentals (SI Edition), *American Society of Heating, Refrigerating and Air-Conditioning Engineers*, Inc.

American Society of Heating Refrigerating and Air-Conditioning Engineers (ASHRAE) (2013). ASHRAE Handbook - Fundamentals (SI Edition), *American Society of Heating, Refrigerating and Air-Conditioning Engineers*, Inc.

Bastidas, A. M. P. (2016). *Ottawa F-65 sand characterization*. University of California, Davis.

Bejan, A. (2013). Convection heat transfer. *John wiley & sons*.

Bergman, T. L., Incropera, F. P., DeWitt, D. P., & Lavine, A. S. (2011). Fundamentals of heat and mass transfer. *John Wiley & Sons*.

Bowers Jr, G. A. (2016). Ground-source bridge deck deicing and integrated shallow geothermal energy harvesting systems [*Doctoral dissertation, Virginia Tech*].

Brandl, H. (2006). Energy foundations and other thermo-active ground structures. *Géotechnique*, 56(2), 81-122.

Chowdhury, M. (2019). Analytical and Numerical Modeling of Externally Heated Geothermal Bridge Deck [*Doctoral dissertation, The University of Texas at Arlington*].

Chapman, W.P. (1952). Design of snow melting system. *Heating and Ventilating*, (49) 4: 95-102.

Duffie, J. A., Beckman, W. A., & Worek, W. M. (1994). Solar engineering of thermal processes.

Frieling, Z.J. (2019). Urease immobilization for advancing enzyme-induced calcium carbonate precipitation applications [*Master's Thesis, Montana State University-Bozeman, College of Engineering*]

Howell, J. R., Mengüç, M. P., Daun, K., & Siegel, R. (2020). Thermal radiation heat transfer. *CRC press*.

Incropera, F. P., DeWitt, D. P., Bergman, T. L., & Lavine, A. S. (2006). Transient conduction. *Fundamentals of heat and mass transfer*, 3, 243-245.

Kim, K. H., Jeon, S. E., Kim, J. K., & Yang, S. (2003). An experimental study on thermal conductivity of concrete. *Cement and concrete research*, 33(3), 363-371.

Kusuda, T., & Achenbach, P. R. (1965). Earth temperature and thermal diffusivity at selected stations in the United States. *National Bureau of Standards Gaithersburg MD*.

Ladd, R. S. (1978). Preparing test specimens using undercompaction. *Geotechnical testing journal*, *1*(1), 16-23.

Levinson, R. & H. Akbari, (2001). Eeffects of composition and exposure on the solar reflectance of Portland cement concrete, LBNL-48334, *Heat Island Group, Environmental Energy*

Technologies Division, Lawrence Berkeley National Laboratory, University of California, Berkeley, CA.

Liu, X. (2005). Development and experimental validation of simulation of hydronic snow melting systems for bridges [*Master's Thesis, Oklahoma State University*].

Martin, M., & P. Berdahl, (1984). Characteristics of infrared sky radiation in the United States. *Solar Energy*, 33(3/4): 321-336.

Price, A. B. (2018). Cyclic strength and cone penetration resistance for mixtures of silica silt and kaolin. [*University of California, Davis*].

Ramsey, J.W, H.D. Chiang, & R.J. Goldstein. (1982). A Study of the Incoming Longwave Atmospheric Radiation from a Clear Sky. *Journal of Applied meteorology*, 21: 566- 578.

Rees, S.J., J.D. Spitler & X. Xiao. (2002). Transient Analysis of Snow-melting System Performance. *ASHRAE Transactions*, 108(2): 406-423.

Sen, S., & Roesler, J. (2019). Thermal and optical characterization of asphalt field cores for microscale urban heat island analysis. *Construction and Building Materials*, 217, 600-611.

Wang, H., & Chen, Z. (2009). Study of critical free-area ratio during the snow-melting process on pavement using low-temperature heating fluids. *Energy Conversion and Management*, 50(1), 157-165.

Welty, J., Rorrer, G. L., & Foster, D. G. (2014). Fundamentals of momentum, heat, and mass transfer. *John Wiley & Sons*.

Williams, G.P. (1973). Heat Requirements of Snow Melting Systems in Canada. Proc., *National Conference on Snow and Ice Control*. Roads and Transportation Association of Canada, Ottawa, April 1973, P. 179-197.